ANNUAL REVIEWS

Annual Review of Fluid Mechanics

Rheology of Active Fluids

David Saintillan

Department of Mechanical and Aerospace Engineering, University of California San Diego, La Jolla, California 92104; email: dstn@ucsd.edu

Keywords

Abstract

An active fluid denotes a viscous suspension of particles, cells, or macromolecules able to convert chemical energy into mechanical work by generating stresses on the microscale. By virtue of this internal energy conversion, these systems display unusual macroscopic rheological signatures, including a curious transition to an apparent superfluid-like state where internal activity exactly compensates viscous dissipation. These behaviors are unlike those of classical complex fluids and result from the coupling of particle configurations with both externally applied flows and internally generated fluid disturbances. Focusing on the well-studied example of a suspension of microswimmers, this review summarizes recent experiments, models, and simulations in this area and highlights the critical role played by the rheological response of these active materials in a multitude of phenomena, from the enhanced transport of passive suspended objects to the emergence of spontaneous flows and collective motion.

Review in Advance first posted on October 23, 2017. (Changes may still occur before final publication.)

1. INTRODUCTION

An active fluid denotes a collection of particles, cells, or macromolecules, typically suspended in a viscous fluid, which are able to convert chemical energy into mechanical work. Examples abound in biology, from motile microorganisms that burn energy from nutrients to achieve locomotion (Lauga & Powers 2009) to the cell cytoskeleton where molecular enzymes powered by ATP (adenosine triphosphate) exert forces on structural filaments, for instance, during cell division (Shelley 2016). Inspired by these living micromachines, materials scientists and engineers have also found ways to design and manufacture active particles in the lab, which sometimes mimic their biological counterparts. In other cases, they have relied on novel propulsion mechanisms such as nonuniform surface chemical reactions (Moran & Posner 2017).

The recent interest in these active systems has been motivated by a variety of factors. On the one hand, deciphering the complex collective dynamics and spontaneous organization that biological active matter often displays might yield a better understanding of fundamental processes in biophysics, from the transport and spreading of bacterial colonies to the biomechanics of individual cells or subcellular units. On the other hand, engineered active suspensions may find uses in a wide range of technological applications, from fluid mixing and pumping to the directed transport of cargo on the microscale, for instance, in lab-on-a-chip devices or for drug delivery (Wang 2013).

Suspensions of active particles exhibit a rich phenomenology, which is very unlike that of passive systems. The mere propulsion of individual microswimmers can result in unusual transport properties such as enhanced diffusion, accumulation near boundaries, and rectification (Elgeti et al. 2015). In more concentrated systems, interactions between particles often result in emergent collective dynamics, such as sustained chaotic turbulent-like motions in the bulk (Sokolov & Aranson 2012) and spontaneous unidirectional flows under confinement (Wioland et al. 2015). The response of active suspensions to external forcing can defy intuition, with rheological measurements in simple flows reporting a peculiar transition to superfluid-like behavior (López et al. 2015).

Underlying many of these phenomena is the internal generation of mechanical energy, which is expended towards locomotion but also drives disturbances in the suspending viscous medium. The coupling of particle configurations with flow, whether externally imposed or self-induced, can thus lead to bizarre rheological behaviors not observed in classic complex fluids. This review summarizes these effects, as well as the models that have been developed to rationalize them. Many other fascinating aspects of active suspensions not directly pertaining to their rheology are not covered; the reader interested in these details is referred to existing reviews (Lauga & Powers 2009, Koch & Subramanian 2011, Marchetti et al. 2013, Elgeti et al. 2015, Saintillan & Shelley 2015, Clément et al. 2016, Lauga & Michelin 2016, Shelley 2016). Finally, this review focuses on the rheology of microswimmer suspensions; other active systems that do not involve self-propelled particles also exhibit interesting rheological properties, and a few examples are briefly discussed in Section 5.

2. MICROSCOPIC DESCRIPTION OF ACTIVE SUSPENSIONS

2.1. Swimming Particles: Mechanisms and Transport

An extensive body of literature exists on the analysis and modeling of single swimmer dynamics. I only mention here a few key aspects that are important to understanding the rheology; more details on swimming mechanisms can be found in previous reviews (Brennen & Winet 1977, Lauga & Powers 2009, Ebbens & Howse 2010, Elgeti et al. 2015, Goldstein 2015, Lauga 2016). Typical microswimmers, with sizes of the order of 1–100 μm and velocities of a few body lengths per second, live in the world of low Reynolds numbers, where inertial effects are negligible and fluid

motions are dominated by viscous forces. The reversibility of the Stokes equations in this case restricts the types of body deformations that enable propulsion to nonreciprocal trajectories in phase space, so as to break Purcell's (1977) celebrated scallop theorem. Flagellated organisms such as many motile bacteria (including *Escherichia coli* and *Bacilus subtilis*), certain types of microalgae (including *Chlamydomonas reinhardtii*), and spermatozoa rely on long, flexible appendages termed flagella, whose nonreciprocal deformations in the form of helical rotations or planar beating motions impart a net thrust on the fluid by taking advantage of the drag anisotropy of slender filaments in Stokes flow (Gray & Hancock 1955, Batchelor 1970b, Lighthill 1975). This thrust balances the drag on other portions of the organism, resulting in a net unidirectional motion at an average speed V_0. Other types of swimmers, such as *Volvox carteri* and *Paramecia*, use arrays of short, hairlike filaments termed cilia, whose biological architecture is very similar to flagella. By undulating these ciliary carpets in a coordinated fashion known as a metachronal wave, these swimmers induce an effective surface flow, which also leads to net propulsion (Blake 2001).

Breakthroughs in materials science and nanofabrication over the last decade have also enabled the design and manufacturing of a multitude of synthetic microswimmers (Ebbens & Howse 2010), relying on a variety of propulsion mechanisms that in some cases mimic those found in biology. Some of the most popular mechanisms involve self-diffusiophoresis using nonuniform surface reactions (Moran & Posner 2017), self-electrophoresis using redox reactions (Paxton et al. 2004), and bubble generation (Gibbs & Zhao 2009), among others. Although some of these particles are very efficient swimmers, the macroscopic characterization of their rheological properties has been lagging, in part due to sedimentation out of suspension and to the difficulty in concentrating these particles without causing aggregation. For these reasons, the discussion centers on biological swimmers, although many of the concepts and models are applicable to both.

Longtime transport properties of microswimmers hinge not only on their ability to self-propel, but also on the importance of orientation decorrelation mechanisms, which tend to randomize orientations and whose coupling with swimming motions results in diffusive random walks in space. The case of swimming *E. coli* was studied in detail by Berg (2004), who observed that periods of nearly straight swimming motions (runs) alternate with fast random reorientation events (tumbles) caused by the unbundling and rebundling of the bacterial flagella (**Figure 1a**). Denoting the direction of swimming by unit vector **p**, these tumbling events can be seen as stochastic changes in **p** occurring with characteristic frequency τ_r^{-1}, where τ_r is the mean duration of a run and is on the order of a second. Assuming pre- and posttumble orientations are uncorrelated, *E. coli* trajectories appear as random walks in space, with an average step length given by the run length $\ell_r = V_0 \tau_r$. A simple calculation (Berg 1993) then predicts a mean-square displacement growing with time as $\langle |\mathbf{r}(t) - \mathbf{r}(0)|^2 \rangle \sim 6 D_{\text{eff}} t$, where $\langle \cdot \rangle$ is the ensemble average. The effective swim diffusivity D_{eff} is found to be $V_0^2 \tau_r / 6$ for a constant run length and $V_0^2 \tau_r / 3$ for an exponentially distributed random run length. In *E. coli*, pre- and posttumble directions are in fact correlated, with an average change in orientation of $58 \pm 40°$ during one tumble (Turner et al. 2000). This correlation can be accounted for by introducing the conditional probability $K(\mathbf{p}'|\mathbf{p})$ for a tumble from orientation **p** to **p**', for which Subramanian & Koch (2009) proposed the following model:
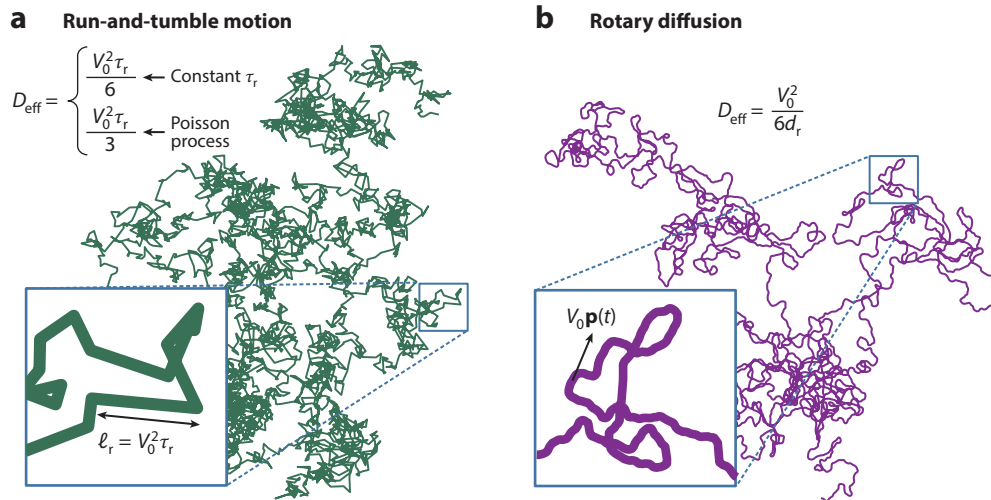
$$K(\mathbf{p}'|\mathbf{p}) = \frac{\xi}{4\pi \sinh \xi} \exp(\xi \mathbf{p} \cdot \mathbf{p}'). \qquad 1.$$

The parameter ξ quantifies the degree of correlation, with $\xi \to 0$ corresponding to uncorrelated tumbling and $\xi \to \infty$ to infinitesimal changes in orientation; the value of $\xi \approx 1.5$ captures the case of *E. coli*. Although the tumbling rate can be assumed to be constant in homogeneous environments, various external gradients can cause spatiotemporal variations in τ_r, which enables

Flagellum: flexible thread-like appendage with a helical polymeric structure used by many microorganisms for locomotion

Drag anisotropy: the drag force on a slender object translating in Stokes flow is twice as large perpendicular to its main axis as it is parallel to it

a   **Run-and-tumble motion**

$$D_{eff} = \begin{cases} \dfrac{V_0^2 \tau_r}{6} & \leftarrow \text{Constant } \tau_r \\[2mm] \dfrac{V_0^2 \tau_r}{3} & \leftarrow \begin{array}{l}\text{Poisson}\\\text{process}\end{array} \end{cases}$$

$$\ell_r = V_0^2 \tau_r$$

b   **Rotary diffusion**

$$D_{eff} = \frac{V_0^2}{6 d_r}$$

$$V_0 \mathbf{p}(t)$$

Figure 1

Random walks resulting from the coupling of self-propulsion and orientation decorrelation mechanisms. (*a*) Run-and-tumble motion, consisting of straight runs of length $\ell_r = V_0 \tau_r$ interspersed with random tumbles occurring with mean frequency τ_r^{-1}. (*b*) Rotary diffusion, in which the particle director performs a random walk on the unit sphere of orientations. Both types of trajectories exhibit linear growth of the mean-square displacements at long times: $\langle |\mathbf{r}(t) - \mathbf{r}(0)|^2 \rangle \sim 6 D_{eff} t$.

bacteria to bias their random walks so as to migrate along the gradient direction, for instance, during chemotaxis (Alt 1980).

In addition to run-and-tumble dynamics, microswimmers are also subject to noise, which results in orientational diffusion. Thermal Brownian motion only plays a weak role in the dynamics of biological swimmers; other sources of noise may include fluctuations in flagellar beating patterns. This orientational diffusion can be characterized by a rotary diffusivity d_r; its coupling with swimming also results in correlated random walks with a linear growth of mean-square displacements (**Figure 1***b*). The effective spatial diffusivity in this case can be calculated using generalized Taylor dispersion theory (Brenner & Condiff 1974, Brenner 1980) as $D_{eff} = V_0^2/6 d_r$. The run length $\ell_r = V_0 d_r^{-1}$ is now interpreted as the persistence length of swimmer trajectories, i.e., the characteristic distance a swimmer will traverse before losing memory of its initial orientation, $\langle \mathbf{p}(s) \cdot \mathbf{p}(s') \rangle \sim \exp(-2|s - s'|/\ell_r)$, where s denotes the arclength along a trajectory. As is well understood in the case of passive Brownian rods (Hinch & Leal 1972, 1976; Brenner 1974; Petrie 1999), the competition between the randomization of particle orientations, either by run-and-tumble dynamics or orientational diffusion, and the alignment imposed by external flows is expected to result in non-Newtonian rheological properties; the finite timescale for the relaxation of particle orientations in unsteady flows also hints at viscoelasticity.

Although sufficient to understand important aspects of suspension rheology, the paradigmatic description of a microswimmer as a self-propelled particle with swimming velocity $V_0 \mathbf{p}(t)$, where the unit director $\mathbf{p}(t)$ undergoes random tumbles or rotary diffusion, omits many details of swimmer dynamics. On shorter timescales, swimmers can, for instance, exhibit unsteady motions due to the periodic strokes they exert for self-propulsion. These effects have been characterized experimentally for *C. reinhardtii* (Guasto et al. 2010, Garcia et al. 2011), where the direction of motion is found to oscillate during one swimming stroke as a result of the back-and-forth beating of the flagella, leading to zigzagging trajectories on very short length scales (Garcia et al. 2011).

2.2. Disturbance Flows

Another key factor in the rheological response of active suspensions, in addition to microswimmer transport properties, is the disturbance flows induced by individual particles. In the case of passive objects, a disturbance velocity only arises if an external force or flow field is imposed; this is unlike self-propelled particles, which drive fluid disturbances even in quiescent environments. The flow field a swimmer generates depends in a complicated manner on body kinematics, surface stresses, and possible surface slip (Lauga & Powers 2009, Lauga 2016). In the Stokes regime of microscopic swimmers, the disturbance flow induced by any particle can be represented in general terms as a linear function of surface tractions and velocities (Pozrikidis 1992):

$$\mathbf{v}(\mathbf{x}) = -\frac{1}{8\pi\eta_0} \int_{\partial V} \mathbf{J}(\mathbf{x} - \mathbf{x}_0) \cdot \mathbf{t}(\mathbf{x}_0) \, \mathrm{d}A_0 + \frac{1}{4\pi} \int_{\partial V} \mathbf{n}(\mathbf{x}_0) \cdot \mathbf{K}(\mathbf{x} - \mathbf{x}_0) \cdot \mathbf{v}(\mathbf{x}_0) \, \mathrm{d}A_0, \qquad 2.$$

where ∂V denotes the surface of the particle with outward unit normal $\mathbf{n}$, and $\mathbf{t} = \mathbf{n} \cdot \boldsymbol{\sigma}$ is the surface traction expressed in terms of the stress tensor $\boldsymbol{\sigma}$ in a fluid with viscosity η_0. The kernels $\mathbf{J}$ and $\mathbf{K}$ are given by the Oseen tensor and its symmetric gradient:

$$J_{ij}(\mathbf{x}) = \frac{\delta_{ij}}{x} + \frac{x_i x_j}{x^3}, \qquad K_{ijk}(\mathbf{x}) = \frac{1}{2}\left(\frac{\partial J_{ij}}{\partial x_k} + \frac{\partial J_{ik}}{\partial x_j}\right) = -3\frac{x_i x_j x_k}{x^5}. \qquad 3.$$

If the position of the point $\mathbf{x}$ where the velocity is evaluated is far from the particle, a Taylor expansion of the Green's functions provides a far-field representation of the flow in terms of multipole moments $\mathbf{M}^{(n)}$ of the tractions and velocities, which drive a superposition of singular flows expressed in terms of $\mathbf{J}$ and its derivatives (Kim & Karrila 2005):

$$\mathbf{v}(\mathbf{r}) \approx \frac{1}{8\pi\eta_0} \sum_{n=0}^{\infty} \nabla^{(n)}\mathbf{J}(\mathbf{r}) : \mathbf{M}^{(n)}. \qquad 4.$$

Positions $\mathbf{r}$ are now measured relative to the particle centroid, and terms of order n in this multipole expansion decay as $1/r^{n+1}$, so that the velocity in the far field is dominated by the first few nonzero moments. Singularities of order $n = 0$ and 1, which are discussed in the sidebar titled Stokes Flow Singularities and sketched in **Figure 2**, involve the Stokeslet ($n = 0$), which represents the net force $\mathbf{F}$ on the fluid, and Stokes doublet ($n = 1$), whose symmetric and antisymmetric parts represent the first symmetric force moment $\mathbf{S}$ (or stresslet) and net torque $\mathbf{L}$ (or rotlet) on the fluid, respectively. Subsequent terms in the multipole expansion involve higher-order moments and are subdominant; they are, however, useful in describing near-field swimmer interactions (Liao et al. 2007), as well as swimmer–wall scattering dynamics (Spagnolie & Lauga 2012). As shown in Section 3, the rheological behavior of the suspensions is primarily governed by the stresslet and rotlet terms.

The expansion of the disturbance flows around particles in terms of Stokes singularities provides a low-order irreducible description of microswimmers (Ghose & Adhikari 2014), where the various moments such as $\mathbf{F}$, $\mathbf{S}$, and $\mathbf{L}$ can be inferred from experiments or models. For a force- and torque-free swimmer ($\mathbf{F} = \mathbf{L} = \mathbf{0}$), which is the case of many motile microorganisms, the leading singularity is the stresslet. If the swimmer is also axisymmetric with director $\mathbf{p}$, symmetry dictates that the tensor $\mathbf{S}$ be of the form $\mathbf{S} = \sigma_0 \mathbf{pp}$, where the scalar stresslet σ_0 is a signed coefficient depending on the details of propulsion. For reasons that become clear below, extensile swimmers with $\sigma_0 < 0$ are often called pushers, whereas contractile particles with $\sigma_0 > 0$ are termed pullers.

The detailed flow fields around individual swimming microorganisms have been measured in a number of studies using particle image velocimetry, as illustrated in **Figure 3**. The case of swimming *E. coli* shown in **Figure 3a** was considered by Drescher et al. (2011), who found that the far-field velocity is well approximated by a stresslet flow with $\sigma_0 \approx -7.98 \times 10^{-19}$ N·m. The

STOKES FLOW SINGULARITIES

Stokeslet

The leading-order term ($n = 0$) in the multipole expansion of Equation 4 is expressed as

$$v_i^{(0)}(\mathbf{r}) = \frac{1}{8\pi\eta_0} J_{ij}(\mathbf{r})M_j^{(0)} = \frac{1}{8\pi\eta_0}\left(\frac{\delta_{ij}}{r} + \frac{r_i r_j}{r^3}\right)M_j^{(0)}, \quad \text{with} \quad M_j^{(0)} = -\int_{\partial V}\sigma_{jk}n_k\,dA = F_j,$$

where $\mathbf{F}$ denotes the net force exerted by the particle on the fluid.

Stresslet and rotlet

At the next order ($n = 1$), the Stokes doublet is given by

$$v_i^{(1)}(\mathbf{r}) = \frac{1}{8\pi\eta_0}\frac{\partial J_{ij}}{\partial r_k}M_{jk}^{(1)}, \quad \text{with} \quad M_{jk}^{(1)} = \int_{\partial V}\left[\sigma_{jl}n_l x_k + \eta_0(v_j n_k + v_k n_j)\right]dA.$$

Decomposing $\mathbf{M}^{(1)}$ into its symmetric and antisymmetric parts yields the alternate form

$$v_i^{(1)}(\mathbf{r}) = \frac{1}{8\pi\eta_0}\left[\left(\frac{r_i\delta_{jk}}{r^3} - 3\frac{r_i r_j r_k}{r^5}\right)S_{jk} + \epsilon_{ijk}L_j\frac{r_k}{r^3}\right],$$

where $\mathbf{S}$ and $\mathbf{L}$ respectively denote the first symmetric force moment (stresslet) and net torque (rotlet) on the fluid:

$$S_{ij} = \int_{\partial V}\left[\frac{1}{2}(\sigma_{ik}x_j + \sigma_{jk}x_i)n_k - \eta_0(v_i n_j + v_j n_i)\right]dA, \qquad L_i = \epsilon_{ijk}\int_{\partial V}\sigma_{jl}x_k n_l\,dA.$$

absence of a Stokeslet is a simple consequence of the density of the cell, which is nearly the same as that of water. The origin of the stresslet is easily rationalized: The rotation of the flagellar bundle results in a net thrust $-F_0\mathbf{p}$, which must balance the viscous drag force $F_0\mathbf{p}$ exerted by the cell body as it translates through the fluid. This extensile force dipole results in a net stresslet with magnitude $\sigma_0 \approx -F_0\ell$, where ℓ is a characteristic length on the order of the cell dimensions and the negative sign of σ_0 is the signature of a pusher, which uses its flagellar tail to push itself
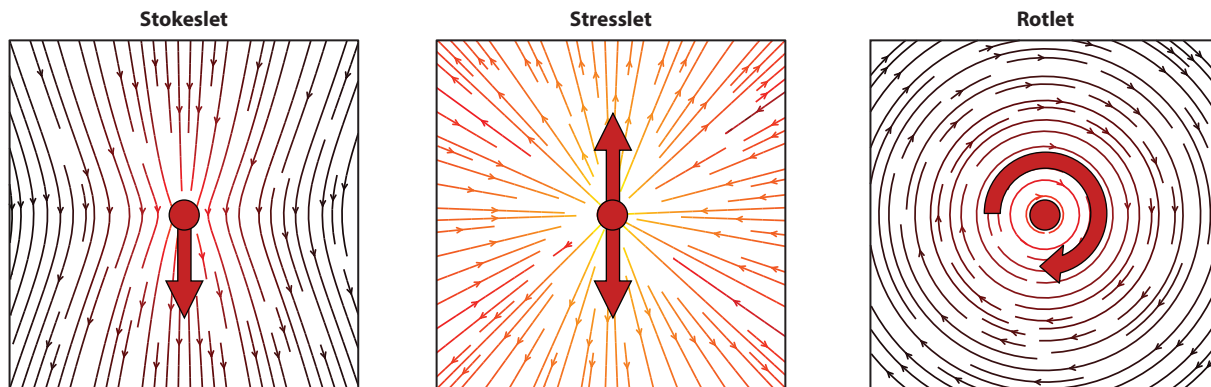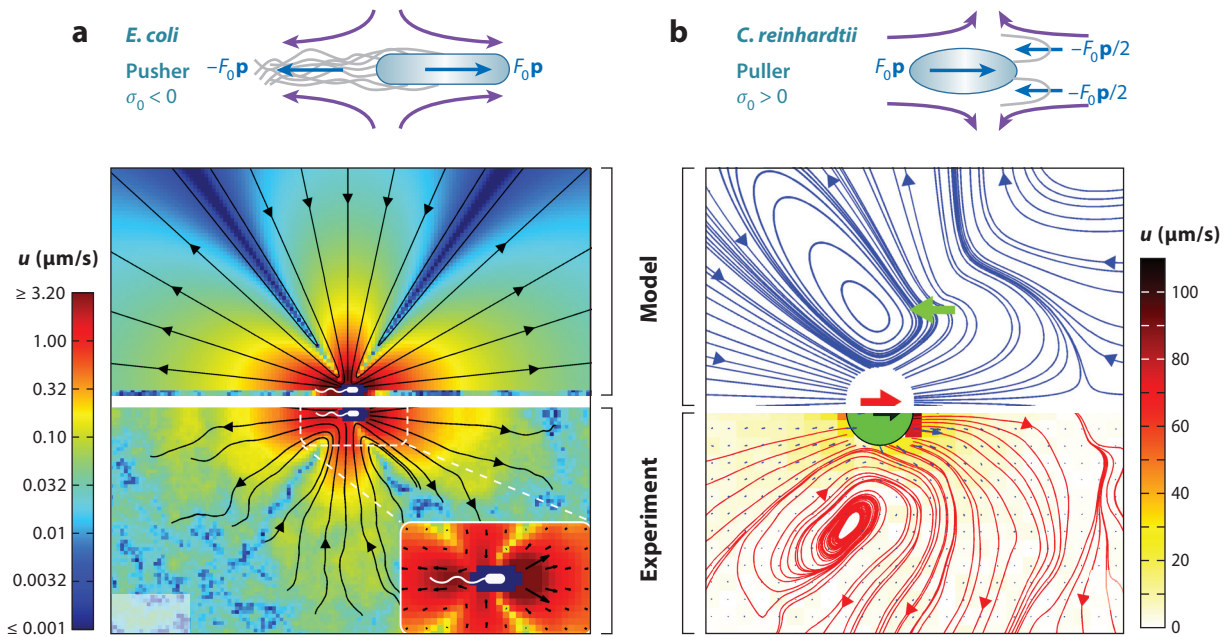

Figure 2

Streamlines driven by Stokeslet, stresslet, and rotlet singularities in Stokes flow. Expressions for the flow fields are provided in the sidebar titled Stokes Flow Singularities.

Figure 3

Disturbance flows induced by swimming microorganisms. (*a*) Drescher et al.'s (2011) particle image velocimetry measurements around individual *Escherichia coli* cells (*bottom*) compared to a theoretical stresslet flow (*top*). (*b*) Drescher et al.'s (2010) time-averaged particle image velocimetry measurements using *Chlamydomonas reinhardtii* show a complex flow in the near field that is well approximated by three off-centered point forces.

through the fluid. Drescher et al. (2011) obtained the values of $\ell = 1.9$ μm and $F_0 = 0.42$ pN, which are consistent with optical trap measurements (Chattopadhyay et al. 2006) and resistive force theory calculations (Darnton et al. 2007). Although the stresslet is shown to capture the single-cell disturbance very well in the far field, significant departures are observed near the cell body where higher-order singularities play a role; in particular, we expect a rotlet dipole (with a decay rate $1/r^3$) to arise due to the equal and opposite torques exerted by the flagellar bundle and cell body as they counter-rotate (Lauga et al. 2006).

The disturbance flow induced by swimming *C. reinhardtii* (**Figure 3b**) was also measured by Drescher et al. (2010) in three dimensions and by Guasto et al. (2010) in quasi-two-dimensional (2D) liquid films. In this case, the flow field shows a complex spatiotemporal dependence in the near field due to the unsteady beating of the two flagella. However, the time-averaged flow is found once again to be dominated by a stresslet, resulting from the equal and opposite thrust and drag forces exerted by the flagella and cell body on the surrounding medium. In this case, the stresslet strength σ_0 is positive, which is the signature of a puller. In the near field, a more faithful representation of the flow field can be achieved using three off-centered point forces capturing the active forces $-F_0\mathbf{p}/2$ on both flagella and the drag force $F_0\mathbf{p}$ on the cell body. As evidenced by Guasto et al.'s (2010) time-resolved measurements, the averaged flow fails to capture many details of the swimming stroke, during which the sign of the stresslet magnitude even reverses (Klindt & Friedrich 2015). The implications of time-dependent strokes on hydrodynamic instabilities and collective motion have been addressed in a few models (Fürthauer & Ramaswamy 2013, Leoni & Liverpool 2014, Brotto et al. 2015), some of which predict the possibility of hydrodynamic synchronization. In dilute systems and in the absence of synchronization, unsteady swimming

is not expected to affect suspension rheology on timescales longer than the stroke period under steady applied flows; its effect in unsteady flows is unclear.

Although the prototypical cases of *E. coli* and *C. reinhardtii* provide a basis for understanding the disturbances induced by typical microorganisms in terms of stresslets, other types of flow singularities become useful in some situations. In particular, nonneutrally buoyant microorganisms are subject to a nonzero Stokeslet, as is the case of *V. carteri*, which is denser than water and swims against gravity (Drescher et al. 2010). Swimmers subject to an external torque, such as gravitactic algae (Pedley & Kessler 1990) and magnetotactic bacteria (Blakemore 1982), can also drive rotlet flows. The flows around autophoretic colloids and other synthetic self-propelled particles have received limited attention; theoretical calculations based on a simple phoretic slip model for spheroidal Janus particles of varying aspect ratios predict both pusher and puller behavior depending on particle shape (Lauga & Michelin 2016).

3. RHEOLOGY: EXPERIMENTS AND MODELS

3.1. Active Hydrodynamic Stress

In this section, we discuss the hydrodynamic contribution to the active rheology, which arises from the stresslet disturbances induced by active particles in the surrounding fluid as a result of self-propulsion. Another distinct contribution to the stress arising from the diffusive character of the swimming motions is discussed in Section 3.2.

3.1.1. Basic mechanism. The disturbance flows induced by active particles can interact with external flows to modify the rheological response of their suspensions. This active contribution to the rheology can be interpreted as an internal active stress of hydrodynamic origin and comes in addition to the basic stress contributions that would arise in flowing suspensions of passive elongated particles (Hinch & Leal 1972, 1976; Brenner 1974; Petrie 1999). Elongated particles are a useful baseline for this discussion because they have a fundamental orientation, just as any active particle must. The basic mechanism for viscosity modification by a suspension of microswimmers, first explained by Hatwalne et al. (2004), is illustrated in **Figure 4** for pusher and puller particles in steady simple shear flow and compared to the case of a passive particle. A slender non-Brownian rod in shear flow undergoes a periodic tumbling motion known as a Jeffery orbit (Jeffery 1922,
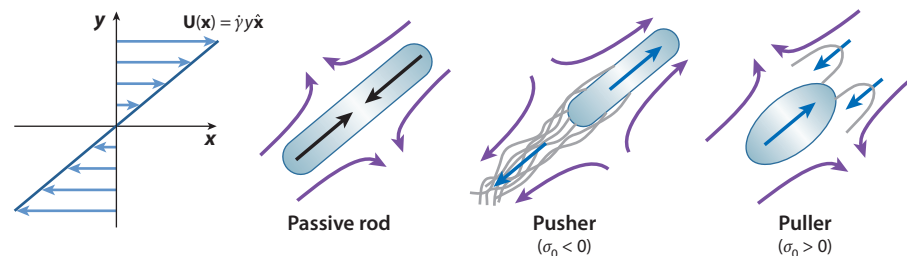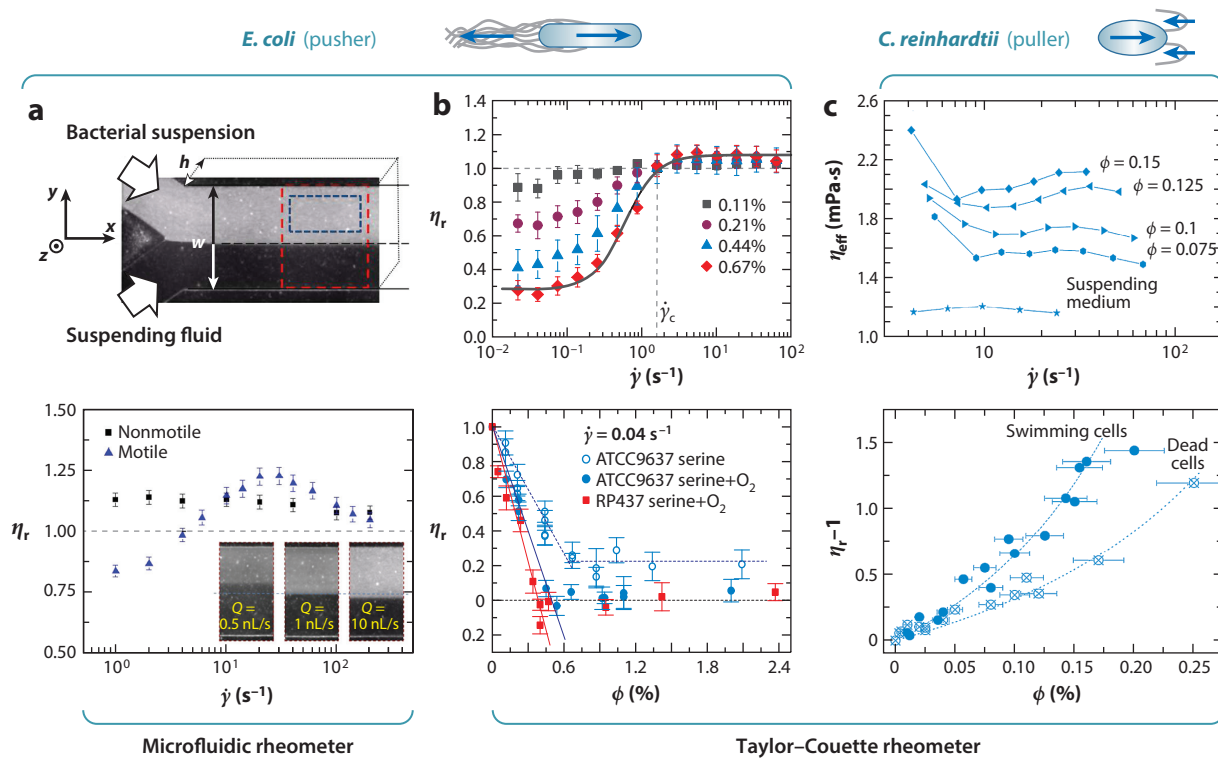

Figure 4

Basic mechanism for the active hydrodynamic contribution to the rheology in a uniform imposed shear flow (Hatwalne et al. 2004, Saintillan 2010b), comparing the case of a pusher and a puller to that of a passive rodlike particle. Flow-induced forces exerted by a passive particle (*black arrows*) and active forces exerted by the swimmers on the fluid as a result of self-propulsion (*blue arrows*) drive disturbance flows (*purple arrows*). In the case of a pusher such as *Escherichia coli* ($\sigma_0 < 0$), the disturbance enhances the applied flow, thus reducing the apparent viscosity; the effect is reversed for a puller such as *Chlamydomonas reinhardtii* ($\sigma_0 > 0$).

Bretherton 1962); during one such orbit, the particle spends most of its time nearly aligned with the flow direction, but with equal amounts of time in the extensional and compressional quadrants. This picture changes qualitatively in the presence of orientation decorrelation mechanisms such as rotational diffusion or run-and-tumble dynamics: Although the shear flow still causes tumbling motions, the orbits are now stochastic with an orientation probability distribution function that peaks in the extensional quadrant, resulting in a mean orientation, such as for the passive rod depicted in **Figure 4** (Chen & Jiang 1999). In this configuration, the particle experiences an extensional flow that tries to stretch it. If the particle is rigid or finitely extensible, this tension is resisted by an induced contractile stresslet that has the net effect of impeding the flow and thus enhances the effective viscosity of the system. In the case of an active swimmer, this mechanism is still present, but the particle exerts in addition a net active stresslet σ_0 due to self-propulsion, whose sign is dictated by the swimming mechanism and is independent of the flow experienced by the swimmer. In the case of an extensile swimmer such as *E. coli*, the active stresslet opposes the passive flow-induced stresslet and drives a disturbance that tends to reinforce the applied flow, thus reducing the shear stress required to drive the flow and decreasing the effective viscosity of the system. The situation is reversed in the case of a contractile swimmer such as *C. reinhardtii*, which drives an active flow that opposes the applied shear and thus increases the effective viscosity. It is interesting to note that an oblate particle should align with its major axis pointing in the compressional quadrant, and the predicted trends should reverse (Bechtel & Khair 2017); common biological and synthetic swimmers have prolate shapes.

3.1.2. Experimental observations. The basic qualitative picture of **Figure 4**, which predicts a decrease in viscosity for pushers and an increase for pullers, has been confirmed in a number of experimental studies, though accurate measurements of the viscosity of active suspensions are technically challenging for two main reasons. Firstly, the viscosities are typically close to that of water (or even less in the case of pusher suspensions), whereas standard commercial rheometers function best with more viscous fluids. Secondly, the effects of activity on the rheology, as explained below, manifest themselves at very low shear rates where the noise in the measurements is most significant. This has prompted experimentalists to design new rheometers to overcome these constraints. The first viscosity measurement in a suspension of swimming microorganisms was performed by Sokolov & Aranson (2009), who confined *B. subtilis* bacteria, which are pushers, in a quasi-2D stabilized liquid film. The viscosity was estimated using two complementary experiments, one based on the timescale for the viscous decay of a macroscopic vortex and the other on torque measurements on a rotating probe immersed inside the film. Both experiments yielded viscosity estimates below that of the solvent at low concentrations, sometimes by up to a factor of 7; the viscosity was then found to increase and exceed that of the solvent at higher densities. However, the unusual geometry and nonviscometric nature of the flow made it difficult to compare these macroscopic estimates with model predictions.

More precise measurements using *E. coli* bacteria were obtained recently by Gachelin et al. (2013) and López et al. (2015) and are summarized in **Figure 5**. Gachelin et al. (2013) devised a microfluidic rheometer based on a Y-shaped junction in a Hele–Shaw geometry (**Figure 5a**), where they measured the deflection of the interface between two coflowing streams with equal flow rates, one of a bacterial suspension and one of a pure solvent, as they meet in the main channel. Assuming a Poiseuille law across the Hele–Shaw gap, this deflection directly provides the relative viscosity η_r between the two fluids. Live bacteria are indeed found to decrease the viscosity below that of the solvent at low flow rates; however, η_r increases with shear rate $\dot{\gamma}$, reaching a maximum above unity before shear thinning again. Suspensions of dead bacteria, however, behave similarly to passive rods with $\eta_r > 1$ and display shear thinning over the whole range of flow

Figure 5

Steady shear experiments. (*a*) Gachelin et al. (2013) used a microfluidic rheometer to measure the relative viscosity η_r of dilute
Escherichia coli suspensions as a function of wall shear rate $\dot{\gamma}$. (*b*) López et al.'s (2015) experiments using *E. coli* in a Taylor–Couette
device showed that η_r decays towards zero with increasing volume fraction ϕ. (*c*) Rafaï et al.'s (2010) Taylor–Couette measurements of
Chlamydomonas reinhardtii suspensions show an increase in viscosity due to activity.

rates (Brenner 1974). López et al. (2015) performed their experiments, shown in **Figure 5b**, in a
conventional Taylor–Couette rheometer specially designed to handle low torques and viscosities.
The relative viscosity in their case displayed similar trends with shear rate, with a low-shear-
rate plateau with $\eta_r^0 < 1$ caused by activity, followed by shear thickening. Increasing the density
of bacteria was found to decrease the value of the plateau towards zero: $\eta_r^0 \to 0$. The measured
viscosity, within experimental uncertainty, actually vanishes in oxygenated suspensions for volume
fractions in excess of 1%. This surprising superfluid-like behavior should not be seen as a violation
of thermodynamic principles, as the bacteria consume chemical energy. Rather, it suggests that the
viscous dissipation in the flowing suspension is macroscopically balanced by the input of energy
from swimming, thus allowing for a sustained flow without any applied torque.

The case of puller swimmers was addressed by Rafaï et al. (2010), who measured the viscosity
of *C. reinhardtii* suspensions over a wide range of volume fractions ($\phi \sim 0$–25%) in a Taylor–
Couette cell (**Figure 5c**). The suspension viscosity was always found to exceed that of the medium
($\eta_r > 1$) and to increase with concentration following an approximate Krieger–Dougherty law
(Krieger & Dougherty 1959), $\eta_r \approx (1 - \phi/\phi_m)^{-\alpha\phi_m}$, where $\phi_m = 0.62$ is the maximum packing
fraction. The effect of activity was highlighted by comparing live and dead samples, where live
suspensions ($\alpha \approx 4.5$) were found to be significantly more viscous than dead ones ($\alpha \approx 2.5$,
similar to passive spheres), as expected for pullers (**Figure 4**). Weak shear thinning was reported

in all suspensions, although the range of shear rates considered was limited. Direct observations of single-cell dynamics were also reported, where live and dead cells showed distinct motions under shear, likely as a result of the interaction of the beating flagella with the flow: Whereas dead cells followed approximate Jeffery orbits, live cells were shown to swim in nearly straight lines with occasional rapid flips. Experiments by Mussler et al. (2013) in a cone-plate rheometer yielded similar results.

A direct comparison of three different types of swimmers was recently performed by McDonnell et al. (2015) in an acoustically driven microfluidic capillary breakup extensional rheometer. They considered suspensions of *Dunaliella tertiolecta* (a marine alga resembling *C. reinhardtii*), *E. coli* bacteria, and mouse spermatozoa; in each case, they compared live and dead cells. The viscosities measured were always above that of the suspending medium, yet the effects of activity in this extensional device were consistent with those predicted and measured in shear flow: Whereas living algae suspensions were more viscous than dead ones, both *E. coli* and sperm appeared less viscous when alive than dead.

Krieger–Dougherty law: common semi-empirical law used to describe the relative viscosity of concentrated sphere suspensions

3.1.3. Continuum kinetic theories. Many of these experimental observations have been rationalized using kinetic models that coarse-grain microscopic swimmer mechanics to provide predictions for the macroscopic stress resulting from the coupling of flow and activity (Marchetti et al. 2013, Saintillan & Shelley 2015). These models, which formalize the heuristic mechanism of **Figure 4**, typically either extend classic theories for rodlike particle suspensions (Hinch & Leal 1972, 1976; Brenner 1974) or rodlike liquid crystals (Ericksen 1962, de Gennes & Prost 2002) to account for the effect of activity. I outline here the suspension models (Saintillan 2010a,b; Alonso-Matilla et al. 2016), which rely on a description of particle configurations based on a probability density function $\Psi(\mathbf{x}, \mathbf{p}, t)$ of finding a particle at position $\mathbf{x}$ with orientation $\mathbf{p}$ at time t (although there is no dependence on $\mathbf{x}$ in a dilute unbounded system, we retain it as it becomes important in confined geometries). Conservation of particles is typically expressed using the Fokker–Planck equation (Doi & Edwards 1986, Subramanian & Koch 2009),

$$\frac{\partial \Psi}{\partial t} + \nabla_x \cdot \mathbf{J}_x + \nabla_p \cdot \mathbf{J}_p = -\frac{1}{\tau_r}\left[\Psi - \int_\Omega K(\mathbf{p}|\mathbf{p}')\Psi(\mathbf{x}, \mathbf{p}', t)\, d\mathbf{p}' \right], \qquad 5.$$

where changes in Ψ arise from translational and orientational fluxes as well as run-and-tumble dynamics. The spatial flux $\mathbf{J}_x$ accounts for propulsion with velocity V_0 in the direction of $\mathbf{p}$, transport by the fluid velocity $\mathbf{v}(\mathbf{x})$ (which in general includes both externally applied flows and swimmer-induced disturbances), and translational diffusion with constant diffusivity d_t:

$$\mathbf{J}_x = [V_0 \mathbf{p} + \mathbf{v}(\mathbf{x})]\Psi - d_t \nabla_x \Psi. \qquad 6.$$

The rotational flux $\mathbf{J}_p$, on the other hand, describes rotation and alignment in the local velocity gradient according to Jeffery's equation (Jeffery 1922, Bretherton 1962),

$$\mathbf{J}_p = \left[\frac{1}{2}\boldsymbol{\Omega} \times \mathbf{p} + \beta(\mathbf{I} - \mathbf{pp}) \cdot \mathbf{E} \cdot \mathbf{p} \right]\Psi - d_r \nabla_p \Psi, \qquad 7.$$

where $\boldsymbol{\Omega} = \nabla \times \mathbf{v}$ is the vorticity, $\mathbf{E} = (\nabla\mathbf{v} + \nabla\mathbf{v}^T)/2$ is the rate-of-strain tensor, and β denotes Bretherton's constant. For a spheroidal particle of aspect ratio r, one finds that $\beta = (r^2 - 1)/(r^2 + 1)$ and $\beta \approx 1$ for a slender swimmer. Rotational diffusion with diffusivity d_r is also included. Equations 6 and 7 assume that the swimmers are force- and torque-free but are easily generalized.

The right-hand side of Equation 5 models run-and-tumble dynamics as a Poisson process causing random stochastic reorientations of the director $\mathbf{p}$ with mean recurrence time τ_r corresponding to the duration of a run (Bearon & Pedley 2000). We assume τ_r to be constant, although allowing it to depend on an external field can be used to model taxis phenomena (Ezhilan et al. 2012, Kasyap

& Koch 2012). Correlations between pre- and post-tumble orientations are captured by $K(\mathbf{p}|\mathbf{p}')$, which was introduced in Section 2.1.

In a dilute suspension ($\phi \to 0$), particle–particle interactions are negligible, and velocity disturbances induced by swimmers thus do not affect the configuration of the suspension, which can be obtained by solving the above equations with $\mathbf{v}(\mathbf{x}) = \mathbf{U}(\mathbf{x})$, where $\mathbf{U}$ denotes the imposed flow. As the volume fraction ϕ increases, the effect of disturbances on the distribution of particles can no longer be neglected, and the total velocity becomes $\mathbf{v}(\mathbf{x}) = \mathbf{U}(\mathbf{x}) + \mathbf{v}_d(\mathbf{x})$, where $\mathbf{v}_d$ is the mean-field disturbance flow, with associated pressure field q_d. In the creeping flow regime, it satisfies the Stokes equations forced by a non-Newtonian particle stress contribution: $\nabla \cdot \mathbf{v}_d = 0$ and $-\eta_0 \nabla^2 \mathbf{v}_d + \nabla q_d = \nabla \cdot \mathbf{\Sigma}^p$. A key aspect of the model, especially for the calculation of rheological properties, is the description of the particle extra stress $\mathbf{\Sigma}^p$, which encapsulates the average effect of the microswimmers on the flow.

The starting point for the modeling of $\mathbf{\Sigma}^p$ is Batchelor's calculation of the average stress tensor in a suspension of particles (Batchelor 1970b), which is outlined in the sidebar titled Particle Extra Stress: Batchelor's Result and generalizes the Kirkwood formula commonly used for molecular systems (Irving & Kirkwood 1950). The key result of Batchelor's theory expresses the mean particle stress inside a volume V as the average particle stresslet; particles subjected to internal rotations also contribute an antisymmetric stress related to the average torque. In the continuum framework used here, the particle stress at a point in a suspension of identical particles can be expressed by identifying the volume average with a local orientational average, yielding

$$\Sigma_{ij}^p(\mathbf{x}, t) = n\langle S_{ij}\rangle + \frac{1}{2}n\epsilon_{ijk}\langle L_k\rangle, \quad \text{where} \quad \langle S_{ij}\rangle = \frac{1}{n}\int_\Omega S_{ij}\Psi(\mathbf{x}, \mathbf{p}, t)\,d\mathbf{p} \qquad 8.$$

and likewise for $\langle L_k\rangle$. Much work has been done to model $\mathbf{\Sigma}^p$ for passive rodlike particles in various external flows (Batchelor 1971, 1974; Hinch & Leal 1972, 1976; Brenner 1974), which requires solving for the particle stresslet. For passive torque-free rods ($\mathbf{L} = \mathbf{0}$), contributions to the stresslet arise from the external flow (**Figure 4**) as well as Brownian rotations; active swimmers are additionally subject to the permanent active stresslet $\sigma_0\mathbf{pp}$ discussed in Section 2.2. For particles with high aspect ratios ($r \gg 1$), these various contributions can be obtained using slender-body theory for Stokes flow (Batchelor 1970a), yielding

$$\text{Flow-induced stress:} \quad \mathbf{\Sigma}^f = \frac{\pi n \ell^3 \eta_0}{6\ln 2r}\left[\langle \mathbf{pppp}\rangle - \frac{\mathbf{I}}{3}\langle \mathbf{pp}\rangle\right] : \mathbf{E}, \qquad 9.$$

$$\text{Brownian stress:} \quad \mathbf{\Sigma}^b = 3nk_B T\left[\langle \mathbf{pp}\rangle - \frac{\langle \mathbf{I}\rangle}{3}\right], \qquad 10.$$

$$\text{Active stress:} \quad \mathbf{\Sigma}^a = n\sigma_0\left[\langle \mathbf{pp}\rangle - \frac{\langle \mathbf{I}\rangle}{3}\right]. \qquad 11.$$

Here, $\mathbf{E}$ is the rate-of-strain tensor of the local flow, and $k_B T$ is the thermal energy unit. The tensors have been made trace free, which only affects the pressure in the Stokes equations. If the particles are not slender, additional terms enter the expression for $\mathbf{\Sigma}^f$ (Hinch & Leal 1976) but are omitted here for brevity. Equations 9–11 demonstrate that the stress is entirely determined by the second and fourth moments, $\langle \mathbf{pp}\rangle$ and $\langle \mathbf{pppp}\rangle$, of orientations. Calculating these moments requires knowledge of the local orientation distribution, which is determined by the balance of transport, alignment by the flow, and diffusion according to the Fokker–Planck Equation 5. In the general case of a nondilute suspension, Equation 5 must be solved concurrently with the Stokes equations, which involve the unknown stress. The determination of the stress simplifies significantly in the dilute limit where $\mathbf{v}_d = \mathbf{0}$. In this case, the distribution of particles is unaffected

PARTICLE EXTRA STRESS: BATCHELOR'S RESULT

A calculation of the particle extra stress in a suspension of force-free particles was provided by Batchelor (1970b), who expressed the average of the Cauchy stress tensor $\boldsymbol{\sigma}$ over a representative volume V as

$$\langle\boldsymbol{\sigma}\rangle = \frac{1}{V}\int_V \boldsymbol{\sigma}(\mathbf{x})\,\mathrm{d}V = -\langle q\rangle\mathbf{I} + \eta_0[\langle\nabla\mathbf{v}\rangle + \langle\nabla\mathbf{v}\rangle^T] + \boldsymbol{\Sigma}^{\mathrm{P}},$$

where $\langle q\rangle$ and $\langle\nabla\mathbf{v}\rangle$ denote the average pressure and velocity gradient, respectively. The non-Newtonian behavior is captured in the contribution $\boldsymbol{\Sigma}^{\mathrm{P}}$, which, upon application of Cauchy's equation $\nabla\cdot\boldsymbol{\sigma} = \mathbf{0}$, can be written as a sum over all the particles α inside volume V. In index notation, one obtains

$$\Sigma^{\mathrm{P}}_{ij} = \frac{1}{V}\sum_{\alpha=1}^N \int_{\partial V_\alpha}\left[\sigma_{ik}x_j n_k^\alpha - \eta_0(v_i n_j^\alpha + v_j n_i^\alpha)\right]\mathrm{d}A = \frac{1}{V}\sum_{\alpha=1}^N S_{ij}^\alpha + \frac{1}{2V}\sum_{\alpha=1}^N \epsilon_{ijk}L_k^\alpha,$$

where $\mathbf{S}^\alpha$ and $\mathbf{L}^\alpha$ denote the stresslet and torque on particle α, respectively:

$$S_{ij}^\alpha = \int_{\partial V_\alpha}\left[\frac{1}{2}(\sigma_{ik}x_j + \sigma_{jk}x_i)n_k^\alpha - \eta_0(v_i n_j^\alpha + v_j n_i^\alpha)\right]\mathrm{d}A, \quad L_i^\alpha = \epsilon_{ijk}\int_{\partial V_\alpha}\sigma_{jl}x_k n_l\,\mathrm{d}A.$$

For force- and torque-free particles, the particle extra stress is therefore simply given by the average particle stresslet. External torques, however, result in an additional asymmetric stress contribution.

by the particle stress and only depends on the known applied flow; the distribution can therefore be obtained by directly solving the Fokker–Planck equation, which then provides the information necessary to estimate $\boldsymbol{\Sigma}^{\mathrm{P}}$ using Equations 9–11.

We illustrate the model predictions by describing the basic case of steady simple shear flow of an unbounded dilute suspension of torque-free particles (Saintillan 2010b): $\mathbf{U}(\mathbf{x}) = \dot\gamma y\hat{\mathbf{x}}$ and $\mathbf{v}_{\mathrm{d}}(\mathbf{x}) = \mathbf{0}$. Translational invariance then dictates that the distribution of particles be uniform in space and only depend on $\mathbf{p}$: $\Psi(\mathbf{x},\mathbf{p},t) = \Psi(\mathbf{p})$, with significant simplifications to the Fokker–Planck equation. Knowledge of $\Psi(\mathbf{p})$ allows for the direct evaluation of the particle stress, from which the relative shear viscosity is inferred as
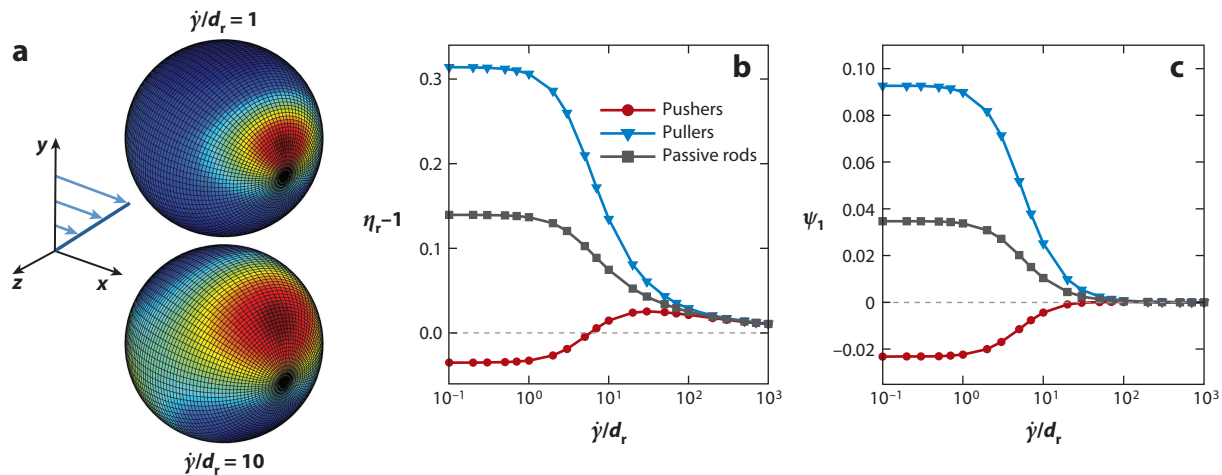
$$\eta_{\mathrm{r}} = \frac{\eta}{\eta_0} = \frac{\sigma_{xy} + \Sigma^{\mathrm{P}}_{xy}}{\eta_0\dot\gamma} = 1 + \frac{\pi n\ell^3}{6\ln 2r}\langle p_x^2 p_y^2\rangle + \frac{3nk_{\mathrm{B}}T + n\sigma_0}{\eta_0\dot\gamma}\langle p_x p_y\rangle. \qquad 12.$$

In the weak-flow limit ($\dot\gamma/d_{\mathrm{r}} \to 0$ and $\dot\gamma\tau_{\mathrm{r}} \to 0$), one can understand the effects of activity by solving for Ψ using a regular asymptotic expansion. In the case of smooth swimmers that do not tumble ($\tau_{\mathrm{r}} \to \infty$), it is straightforward to show that $\langle p_x^2 p_y^2\rangle \to 1/15$ and that $\langle p_x p_y\rangle \to \beta\dot\gamma/30d_{\mathrm{r}}$, yielding the low-shear-rate viscosity estimate

$$\eta_{\mathrm{r}}^0 = \lim_{\dot\gamma\to 0}\eta_{\mathrm{r}} = 1 + \frac{\pi n\ell^3}{30\ln 2r}\left[\underbrace{\left(\beta + \frac{1}{3}\right)}_{\text{passive}} + \underbrace{\beta\frac{\sigma_0}{k_{\mathrm{B}}T}}_{\text{active}}\right], \qquad 13.$$

where we have used the rotational diffusivity of a Brownian rod: $d_{\mathrm{r}} = 3k_{\mathrm{B}}T\ln 2r/\pi\eta_0\ell^3$ (Doi & Edwards 1986). The first term on the right-hand side simply corresponds to the solvent viscosity. The second term, which is always positive, captures the zero-shear-rate particle contribution to the viscosity in a suspension of passive rods. Finally, the third term, which describes the effect of activity, involves the swimming stresslet σ_0 and can be either positive or negative. In suspensions of pullers ($\sigma_0 > 0$), activity always increases η_{r}, whereas it tends to decrease η_{r} in

Figure 6

Model predictions for dilute suspensions of smooth swimmers (no run and tumble, $\tau_r \to \infty$) in steady simple shear flow.
(*a*) Orientation distributions at two distinct flow strengths: $\dot{\gamma}/d_r = 1$ (*top*) and $\dot{\gamma}/d_r = 10$ (*bottom*). Typical dependence of (*b*) relative particle viscosity $\eta_r - 1$ and (*c*) first normal-stress difference coefficient ψ_1 on dimensionless flow rate $\dot{\gamma}/d_r$ for pushers, pullers, and passive rods. Adapted from Saintillan (2010b).

suspensions of pushers ($\sigma_0 < 0$). If active stresses dominate passive contributions from the flow and Brownian rotations, Equation 13 predicts a linear decrease of the viscosity with increasing volume fraction in suspensions of pushers. This is in agreement with experimental observations (**Figure 5b**) and predicts a transition to superfluid-like behavior above a critical concentration of $n\ell^3 = -90 \ln 2r/[\pi(1 + 3\beta + 3\beta\sigma_0/k_B T)]$. Of course, this estimate is based on a dilute assumption, and particle–particle interactions are likely to play a role in experimental systems before the transition is reached.

For arbitrary flow strengths, the Fokker–Planck equation must be solved numerically, for instance, by finite differences (Chen & Jiang 1999) or spectral methods (Chen & Koch 1996, Saintillan 2010b). As expected, typical orientation distributions in **Figure 6a** exhibit a peak in the extensional quadrant, which becomes sharper and tends to align towards the flow direction with increasing shear rate. As a result, both $\langle p_x^2 p_y^2 \rangle$ and $\langle p_x p_y \rangle$ tend to decrease with increasing $\dot{\gamma}$. This decrease underlies the shear thinning of suspensions of passive rods and of pullers (**Figure 6b**). In suspensions of pushers, it leads to a complex dependence of the viscosity on flow strength: Even when active stresses dominate at low shear rates so that $\eta_r < 0$, they decay more rapidly than passive stresses with increasing flow strength, resulting in an increase in η_r to a value above unity. At very high shear rates, all stresses decay again, leading to shear thinning. All of these trends are consistent with the experimental observations of Gachelin et al. (2013) and López et al. (2015) (**Figure 5**). The same model can also be used to estimate normal-stress difference coefficients (Saintillan 2010b). The case of $\psi_1 = [\Sigma_{xx}^p - \Sigma_{yy}^p]/\dot{\gamma}^2$ is illustrated in **Figure 6c**, where $\psi_1 > 0$ for passive rods and pullers; the sign of ψ_1 is reversed in pusher suspensions. Similar trends are observed on $\psi_2 = [\Sigma_{yy}^p - \Sigma_{zz}^p]/\dot{\gamma}^2$, albeit with opposite signs. There are no experimental data on these quantities.

Several variants of the dilute model presented here have also been proposed (Haines et al. 2009, Moradi & Najafi 2015), yielding similar conclusions; similar predictions also apply to 2D and 3D extensional flows (Saintillan 2010a), where analytical solutions for the relative viscosity and normal-stress difference coefficients exist for all strain rates. Other models have used a complementary

approach based on phenomenological equations for liquid crystals (Ericksen 1962, de Gennes & Prost 2002), which can be extended to account for activity (Simha & Ramaswamy 2002, Hatwalne et al. 2004, Ramaswamy 2010, Marchetti et al. 2013). One feature that distinguishes these theories from the one described above is that an elastic energy associated with steric interactions was generally included, which provided a mechanism for nematic alignment of the particles even in the absence of flow. Negative viscosities in extensile suspensions were also predicted by these studies (Giomi et al. 2010, Heidenreich et al. 2011), which additionally suggested that the nonmonotonic behavior of $\eta(\dot{\gamma})$ may give rise to shear banding and hysteresis.

3.1.4. Unsteady flows and linear viscoelasticity. Although most experimental measurements and theoretical models have focused on the steady-flow rheology, we anticipate the competition between flow alignment and orientational relaxation by run-and-tumble and rotary diffusion producing viscoelastic behavior in unsteady flows. López et al.'s (2015) experiments using *E. coli* bacteria in a Taylor–Couette rheometer also analyzed the transient stress response upon startup and cessation of shear flow, and these data are summarized in **Figure 7**. Whereas the steady plateau reached after the transient simply corresponds to the steady viscosity measurements of **Figure 5b**, the unsteady response is unusual and exhibits stress overshoots followed by relaxation, which are indicative of elasticity. The deduced stress relaxation time τ_s is found to be nearly constant and on the order of a few seconds, which is consistent with the timescale for relaxation of orientations due to run-and-tumble dynamics; a decrease of τ_s with concentration is observed in the semi-dilute regime. The shape of the transient in these experiments was recently explained by Nambiar et al. (2017): Upon startup of rotation, an initial viscous stress jump occurs primarily due to the solvent viscosity; after this initial jump, particle orientations relax on a timescale of τ_s, leading to a decrease in the measured viscosity as a result of the extensile stresslet $\sigma_0 < 0$; when rotation stops, the negative active stress persists for a duration on the order of τ_s, leading to a negative undershoot in the stress response, which corresponds to a retrograde torque. Nambiar
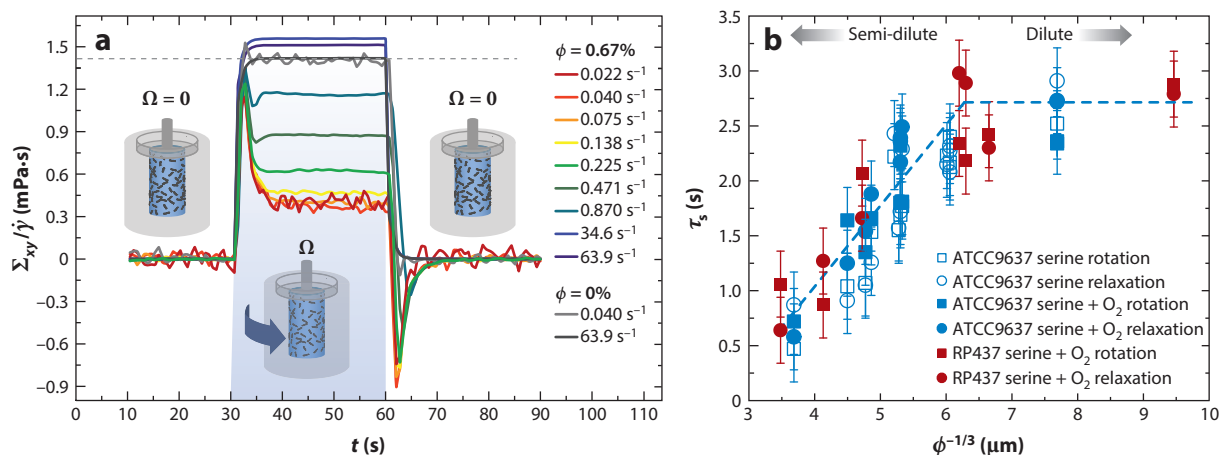

Figure 7

Transient rheological measurements in *Escherichia coli* suspensions in a Taylor–Couette device. (*a*) Transient shear stress $\Sigma_{xy}(t)$ normalized by the applied shear rate $\dot{\gamma}$ upon startup and cessation of rotation, showing (*gray lines*) pure fluid ($\phi = 0$) and (*colored lines*) a bacterial suspension ($\phi = 0.67\%$). (*b*) Stress relaxation time τ_s, obtained by fitting an exponential to the stress response, as a function of the mean distance $\phi^{-1/3}$ between particles. Open and closed symbols denote deoxygenated and oxygenated conditions, respectively. Blue and red symbols correspond to two distinct *E. coli* strains. Adapted from López et al. (2015).

et al. (2017) also developed a transient kinetic model similar to that of Section 3.1.3, which showed good agreement with the observed stress profiles.

The unsteady rheological response can also be understood using linear viscoelasticity theory, which predicts the viscous and elastic components of the complex particle viscosity, $\eta_p^*(\omega) = \eta_p' + i\eta_p''$, in a small-amplitude oscillatory shear flow $\dot{\gamma}(t) = \dot{\gamma}_0 \cos \omega t$ as

$$\frac{\eta_p'}{\eta_0} = 1 + \frac{\pi n \ell^3}{30 \ln 2r} \left[\frac{1}{3} + \frac{\beta}{1+\overline{\omega}^2} \left(1 + \frac{\sigma_0}{k_B T} \right) \right], \quad \frac{\eta_p''}{\eta_0} = \frac{\pi n \ell^3}{30 \ln 2r} \frac{\beta \overline{\omega}}{1+\overline{\omega}^2} \left(1 + \frac{\sigma_0}{k_B T} \right), \quad 14.$$

where $\overline{\omega} = \omega/6d_r$ and where we assumed smooth high-aspect-ratio swimmers subject to Brownian rotational diffusion; generalizations of this result to run-and-tumble particles and nonslender shapes were derived by Nambiar et al. (2017) and Bechtel & Khair (2017), respectively. In the low-frequency limit ($\overline{\omega} \to 0$), the expression for η_p' agrees with the steady weak-flow result of Equation 13. In fact, Bechtel & Khair (2017) verified a modified Cox–Merz rule, where the frequency-dependent linear viscosity approximately matches the steady shear viscosity at the maximum shear rate: $\eta_p'(\omega) \approx \eta_p(\dot{\gamma}_0)$. The elastic component $\eta_p''(\omega)$ is nonzero and peaks at intermediate frequencies, as could have been anticipated from the case of rigid rods; however, its sign can be negative in the case of pushers, which is at the origin of the stress undershoot after the cessation of rotation in **Figure 7a**. Nonlinear effects in finite-amplitude unsteady flows were also recently analyzed by Bozorgi & Underhill (2014), who derived expressions for the first few intrinsic nonlinear material functions in large-amplitude oscillatory shear flow (Ewoldt & Bharadwaj 2013).

3.1.5. Effect of geometry: accumulation and migration. A defining feature of swimmer suspensions is the strong effect of geometry and confinement on the distribution of particles, which tend to accumulate near boundaries. Although the details of swimmer–wall interactions can vary, this accumulation is ubiquitous in suspensions of bacteria (Berke et al. 2008, Figueroa-Morales et al. 2015, Bianchi et al. 2017) as well as sperm (Denissenko et al. 2012), where concentrations near walls can exceed bulk concentrations by several factors. A variety of effects can explain these distributions (Schaar et al. 2015), including kinematic and hydrodynamic mechanisms. In the absence of hydrodynamic interactions, the continuum model of Section 3.1.3, subject to a no-flux condition at the walls, predicts accumulation as a consequence of the balance of self-propulsion and diffusive processes over a boundary layer of thickness $\theta = \delta/\sqrt{2(1 + (\ell_r/\delta)^2/6)}$, where $\ell_r = V_0 d_r^{-1}$ is the run length and $\delta = \sqrt{d_t/d_r}$ is a purely diffusive length scale on the order of particle size (Ezhilan & Saintillan 2015, Yan & Brady 2015). Swimmer–wall hydrodynamic interactions also influence accumulation, which is enhanced in the case of pushers but reduced for pullers (Berke et al. 2008, Spagnolie & Lauga 2012).

Nonuniform particle distributions have also been reported under flow. In strong pressure-driven flows, both experiments (Rusconi et al. 2014) and models (Bearon & Hazel 2015, Ezhilan & Saintillan 2015) show the formation of a depletion layer near the channel centerline, with an accumulation of particles in high-shear near-wall regions. In nonuniform channels, accumulation is observed downstream of constrictions (Altschuler et al. 2013). Several other migration phenomena specific to microswimmers have also been reported, including upstream swimming in pressure-driven flows (Kaya & Koser 2012), rheotaxis under shear due to the chirality of the flagellar bundle (Marcos et al. 2012), and the preferential swimming of microalgae along the vorticity axis in both steady (Chengala et al. 2013) and unsteady flows (Hope et al. 2016). Although the full consequences of these effects on the rheology have yet to be analyzed, the simple case of pressure-driven channel flow was addressed by Alonso-Matilla et al. (2016) using the model of Section 3.1.3. Similar trends as in uniform shear were observed, with a predicted transition to superfluidity. The

accumulation of swimmers in high-shear near-wall regions was shown to have a quantitative effect on the viscosity by enhancing the particle contribution to the stress.

3.1.6. Microrheology and vanishing drag. The rheological behavior of the suspensions also has direct implications for the transport of passive suspended objects, whether freely suspended or driven by an external force. In a Newtonian viscous fluid, the linearity of the Stokes equations at low Reynolds numbers prescribes a linear relation between the forces and torques on a particle and its linear and angular velocities (Guazzelli & Morris 2012):

$$
\begin{bmatrix} \mathbf{F}^{\mathrm{ext}} + \mathbf{F}^{\mathrm{br}} \\ \mathbf{T}^{\mathrm{ext}} + \mathbf{T}^{\mathrm{br}} \end{bmatrix} = \eta_0 \mathbf{R} \cdot \begin{bmatrix} \mathbf{U} \\ \Omega \end{bmatrix},
\tag{15.}
$$

where $\eta_0 \mathbf{R}$ is the shape-dependent resistance tensor. Clearly, we should not expect Equation 15 to apply to a particle suspended in an active suspension, due to viscoelastic and shear-thinning/-thickening properties that render the resistance problem nonlinear and to the importance of geometry on the rheology. Nonetheless, we can expect that an effective decrease in viscosity due to the presence of pushers would result in the faster motion of a probe under a given force and in seemingly more intense thermal fluctuations. The apparent transition to superfluidity may even allow for frictionless translational or rotational motion in the absence of external forces or torques by a symmetry-breaking mechanism reminiscent of that predicted for symmetric phoretic colloids (Michelin et al. 2013). Finally, the elastic character of the response to shear may result in velocity overshoots in which a forced probe keeps translating for a finite time after the force is turned off; this effect would be the active counterpart of the elastic recoil that would be observed in a passive viscoelastic gel.

Detailed active microrheology experiments, under either oscillatory or steady forcing, could confirm some of these predictions but have yet to be performed. The motion of freely suspended passive probes nonetheless offers some insight into these effects. Since the work of Wu & Libchaber (2000), it is well known that passive spheres placed in a bacterial bath exhibit enhanced diffusion as a result of both direct scattering interactions with individual bacteria and transport in the fluid flows induced by swimmer motions. Steady directional motion of symmetric swimmers without external force has not yet been observed; however, mean-square displacements of random probe motions typically exhibit superdiffusive growth at short times, which is indicative of directed motion on short timescales. The nonmonotonic dependence of the long-time diffusivity with probe size also suggests a complex non-Stokesian mechanism for drag (Patteson et al. 2016). Unusual couplings between translational and rotational motions that are not permitted by Equation 15 have also been observed with ellipsoidal probes (Peng et al. 2016). The directed translational or rotational motion of passive objects can be forced by breaking the fore–aft or clockwise symmetry, respectively—for instance, using wedges (Kaiser et al. 2014) or gears (Di Leonardo et al. 2010). The motion in these examples derives primarily from direct interactions with the swimmers (Yan & Brady 2015) rather than from a hydrodynamic transition to superfluid-like behavior.

Models and simulations of passive or driven motions of passive objects in active fluids have been scarce. An active nematic model by Foffano et al. (2012b) did reproduce some of the effects discussed above, including the nonlinear dependence of drag on probe size and a transition to negative apparent drag as a result of activity. However, the anchoring boundary conditions used for swimmer orientations on the surface were found to have a strong effect on the results; in an actual experiment, orientations are typically unconstrained and in fact adjust to the local flow. As expected based on the strong effect of geometry on swimmer configurations, the viscosity calculated numerically in a microrheology model did not match that obtained in simple shear flow (Foffano et al. 2012a).

3.1.7. Effects of concentration. The effects of microswimmer density on the rheology of puller suspensions is relatively simple, with experiments using *C. reinhardtii* showing a monotonic increase of the relative viscosity with density from dilute to dense concentrations (Rafaï et al. 2010). The case of pusher suspensions, however, is still not fully understood. In fairly dilute suspensions under uniform shear, increasing density has the effect of amplifying the particle stress, thus reducing the viscosity in weak flows and enhancing it in strong flows (**Figure 5**). In a Taylor–Couette device, this decrease in viscosity leads to an apparent transition to frictionless flow (López et al. 2015), with spontaneous directed motion in the absence of external forcing (Section 4.2). Other experiments (Sokolov & Aranson 2009, Gachelin et al. 2013), however, report a nonmonotonic dependence on density, with the viscosity reduction observed in weak flows giving way to an increase at high concentrations. In very dense suspensions, the emergence of bacterial turbulence (Section 4.1) leads to a complex rheology (Karmakar et al. 2014), with unexpected trends with respect to shear rate that are likely due to the interaction of the applied flow with the large-scale collective motions (Alizadeh & Saintillan 2011, Saracco et al. 2011, Clément et al. 2016, Secchi et al. 2016).

Deriving kinetic theories to account for concentration effects is challenging owing to particle–particle interactions. Continuum models for semidilute suspensions, some based on renormalization theory (Gyrya et al. 2011, Gluzman et al. 2013), have been limited; one interesting conclusion of these two studies is the role of interactions, which provide an additional mechanism for orientation decorrelation and thus affect the rheology via the mean orientation distribution. Numerical simulations of discrete swimmer suspensions have been more successful at investigating this regime (Ishikawa & Pedley 2007, Gyrya et al. 2011, Pagonabarraga & Llopis 2013, Potomkin et al. 2016) and have been able to capture the nonmonotonic dependence of η on density (Ryan et al. 2011).

3.2. Active Swim Stress

An additional mechanism for stress production in suspensions of self-propelled particles was very recently uncovered by Takatori & Brady (2017). The origin of this stress is not hydrodynamic, but rather stems from the effective diffusion of the swimmers. In the absence of flow, we saw in Section 2.1 that a microswimmer subject to either run-and-tumble dynamics or rotary diffusion performs a random walk in space, with the long-time diffusivity D_{eff} given by either $V_0^2 \tau_r/6$ or $V_0^2/6d_r$, respectively. In an unbounded domain, a cloud of microswimmers therefore spreads diffusively as the particles swim away; in confinement, this diffusive motion instead gives rise to an effective pressure on the container boundaries, which is not unlike the osmotic pressure exerted by Brownian solutes. This so-called swim pressure (Takatori et al. 2014, Solon et al. 2015) can be calculated from the trace of the swim stress, which is provided by the virial theorem as the first moment of a swim force $\mathbf{F}^s$: $\mathbf{\Sigma}^s = -n\langle \mathbf{x}\mathbf{F}^s \rangle$. Here, $\mathbf{F}^s$ should be interpreted as the negative of the force one needs to apply to hold a swimmer fixed in space and depends linearly on its velocity: $\mathbf{F}^s(t) = \zeta \mathbf{V}(t)$, where ζ is the translational friction coefficient of the swimmer. Simple manipulations then yield the expression

$$\mathbf{\Sigma}^s = -n\zeta \int \langle \mathbf{V}(t')\mathbf{V}(t) \rangle \, dt' = -n\zeta \mathbf{D}_{\text{eff}}, \qquad 16.$$

which directly relates the swim stress to the effective diffusion tensor via the Green–Kubo formula. In an isotropic system, this reduces to $\mathbf{\Sigma}^s = -\Pi_s \mathbf{I}$, with a scalar swim pressure $\Pi_s = n\zeta D_{\text{eff}}$. This pressure manifests itself, for instance, by driving the spontaneous motion of passive asymmetric objects immersed in microswimmer baths (Di Leonardo et al. 2010, Kaiser et al. 2014, Yan & Brady 2015).
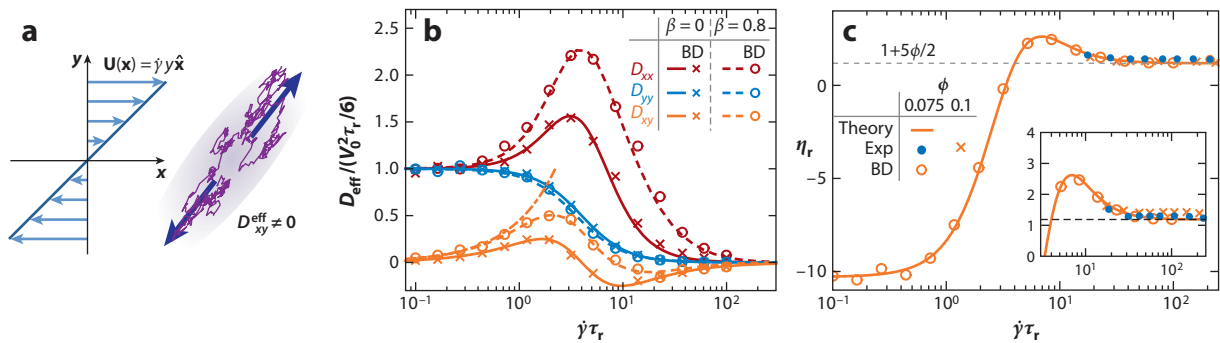
Figure 8

Rheological consequences of the active swim stress. (*a*) In a shear flow, the effective diffusive motion of a swimming particle undergoing run-and-tumble or orientation diffusion is anisotropic and tends to stretch the fluid along the straining direction. (*b*) Dependence of the effective diffusivity tensor on shear rate for both spherical ($\beta = 0$) and prolate ($\beta = 0.8$) swimmers. (*c*) Effective viscosity in suspensions of pullers predicted by theory and Brownian dynamics (BD) simulations is compared to Rafaï et al.'s (2010) experimental results. Adapted from Takatori & Brady (2017).

In a sheared suspension, the coupling of the straining motion with swimming and rotational dynamics results in an anisotropic diffusion tensor, which can also be obtained using generalized Taylor dispersion theory (Brenner 1980, Manela & Frankel 2003, Takatori & Brady 2017). The effect of the shear in weak flows is to bias the random walk of swimmers towards the extensional quadrant, as illustrated in **Figure 8a**, which causes the diffusive stress to effectively stretch the fluid along this direction, thus reducing the apparent viscosity. This is confirmed by a calculation of D_{xy}^{eff}, which is indeed positive in weak flows but becomes negative in strong flows (**Figure 8b**). Viscosity trends qualitatively similar to those found in pusher suspensions as a result of active extensile stresses are therefore anticipated. Furthermore, an interesting prediction of the model is that the swim stress is independent of swimmer type (pusher versus puller) and even arises in sphere suspensions. In particular, Takatori & Brady (2017) anticipate that even puller suspensions should exhibit a viscosity reduction under very weak forcing (**Figure 8c**), though as yet there exist no experimental data at sufficiently low shear rates to test this prediction.

4. HYDRODYNAMIC INSTABILITIES AND SPONTANEOUS FLOWS

4.1. Bulk Instabilities and Collective Motion

Dense suspensions of pushers, and in particular bacterial suspensions, are well known to display emergent collective motions (Koch & Subramanian 2011). This so-called bacterial turbulence, which is internally driven by particle activity, has been characterized in detail in experiments (Cisneros et al. 2007, Sokolov & Aranson 2012) and simulations (Saintillan & Shelley 2012), which both exhibit unsteady vortices, jets, and swirls on length scales much greater than particle dimensions and with typical velocities also exceeding those of isolated swimmers. These chaotic motions are accompanied by unsteady microstructural changes, with swimmers tending to concentrate and align with their neighbors. A vast number of models have been developed to address this phenomenon, as reviewed, for instance, by Marchetti et al. (2013) and Saintillan & Shelley (2015). Both steric interactions between slender swimmers and long-ranged hydrodynamic interactions driven by active stresslets are thought to be responsible for the motions. Hydrodynamic theories have been based on stability analyses of the uniform isotropic base state and predict

a longwave instability resulting from the coupling of active stresses and particle orientations (Saintillan & Shelley 2008, Baskaran & Marchetti 2009). More precisely, a weak-plane wave velocity perturbation induces nematic alignment of slender swimmers along the extensional axis of the flow, which tends to reinforce the initial velocity perturbation via active stresses in the case of pushers; no such instability occurs for pullers. An alternate interpretation, proposed by Subramanian & Koch (2009), is in terms of the apparent viscosity of the system, which is observed to become negative at the marginal stability limit. The emergence of spontaneous flows as viscosity approaches zero should not come as a surprise: Any infinitesimally weak flow disturbance experiencing zero apparent resistance will amplify until a nonlinear flowing state is achieved in which viscous dissipation in the solvent balances the active power input generated by the coordinated swimming motions (Saintillan & Shelley 2015).

4.2. Spontaneous Flows in Confinement

Recent experiments and models have shown that the chaotic flows observed in bulk suspensions can be stabilized by confinement, leading to regular spontaneous flow patterns controlled by geometry. The simple case of a circular domain was analyzed experimentally by Wioland et al. (2013), using a dense *E. coli* suspension in a drop squeezed between two coverslips. After a transient, bacteria spontaneously organized into a steady vortex surrounded by a thin counterrotating boundary layer in the periphery of the drop. This effect was also observed in discrete simulations (Lushi et al. 2014), which underscored the role of stresslet disturbances in driving the vortex flow. Bacteria were found to swim against the net induced flow by an effect similar to upstream swimming, leading to an apparent counterrotation near the boundary. The kinetic theory of Theillard et al. (2017) also produced similar results and explained the transition to the double vortex as a linear instability of the equilibrium quiescent state due to mean-field hydrodynamic interactions.

Directed spontaneous flows have also been observed in periodic channels. Wioland et al.'s (2015) experiments using *E. coli* in racetrack geometries displayed a symmetry-breaking bifurcation leading to flow in an arbitrary direction (**Figure 9a**). This flow was unidirectional in narrow channels, but sinusoidal streamlines with traveling waves emerged with increasing channel width, ultimately leading to chaotic motions. The imaging of individual bacteria demonstrated once again their propensity to align against the self-induced flow, which is driven by the coordinated swimming activity. The case of dense sperm suspensions was also studied by Creppy et al. (2016) in circular channels, where spontaneous net pumping also occurred above a critical sperm density. Using a continuum model, Theillard et al. (2017) simulated spontaneous flows in circular annuli (**Figure 9b**) and captured the same phenomenology as in experiments. The initial transition to flow was again explained as a linear instability of the equilibrium state; interestingly, the marginal stability limit was also shown to match the transition to apparent superfluidity predicted in Poiseuille flow by Alonso-Matilla et al. (2016) in the zero-shear-rate limit. Spontaneous flows are also predicted by kinetic models of active nematics in both straight (Hemingway et al. 2015) and circular (Fürthauer et al. 2012) channels, although the role played by anchoring boundary conditions in these theories is unclear. Using one such model, Fürthauer et al. (2012) suggested that the active power driving spontaneous flows in a Taylor–Couette device might be harnessed to drive a motor, should one of the two cylinders be fixed and the other free to rotate; this prediction is supported in principle by López et al.'s (2015) measurements in a Taylor–Couette rheometer, where finite torques were measured in the absence of any imposed rotation in the superfluid-like regime. As a final comment, we emphasize the importance of boundary conditions on the emergence of these flows. That the transition to zero apparent viscosity was observed by López et al. (2015) and Wioland et al. (2015) but not by Gachelin et al. (2013) may be a consequence of the
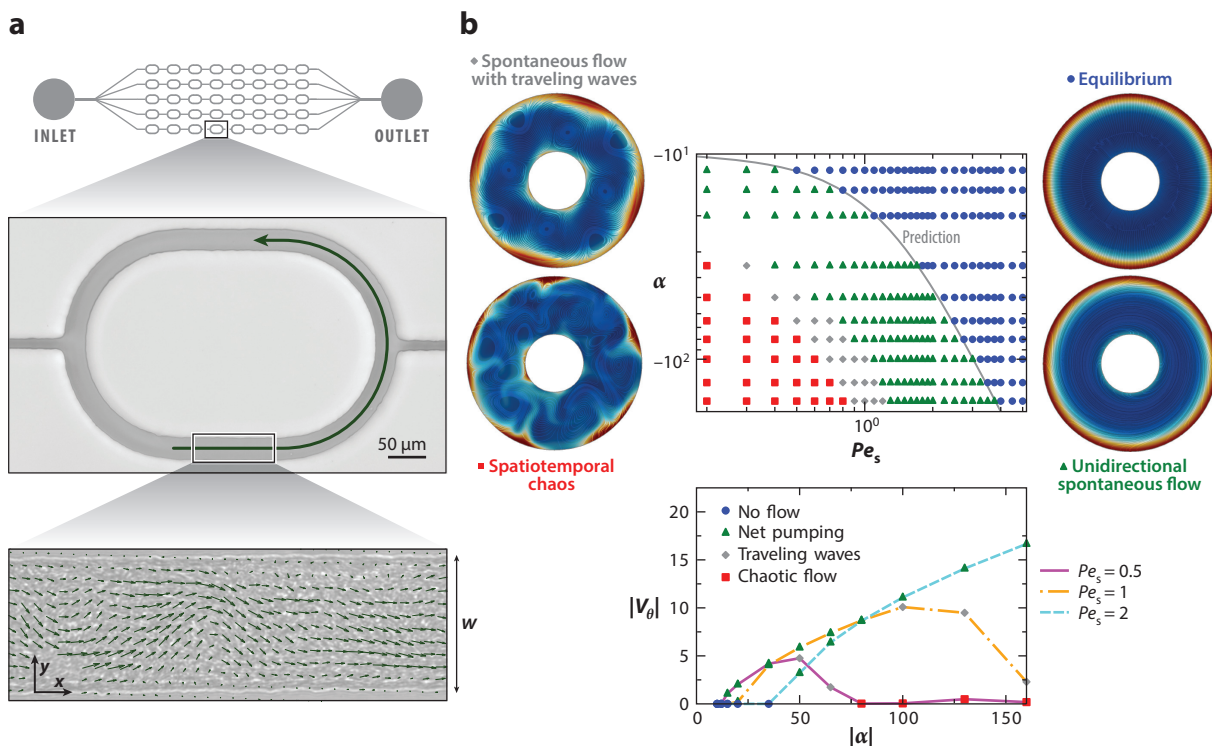
Figure 9

Spontaneous flows of pusher suspensions in periodic channels. (*a*) Wioland et al.'s (2015) experiments showing spontaneous flows in *Escherichia coli* suspensions confined inside microfluidic racetracks. (*b*) Theillard et al.'s (2017) kinetic model and simulations inside an annulus. Increasing activity ($\alpha = n\sigma_0/\eta_0 d_r < 0$ for pushers) or decreasing confinement ($Pe_s = V_0/d_r H$, where H denotes channel width) causes a transition from equilibrium to spontaneous azimuthal flow with net flow rate $|V_\theta|$. Traveling density waves eventually appear followed by spatiotemporal chaos. The dark gray curve shows a theoretical linear prediction for the marginal stability limit of the equilibrium state; it also matches the transition to superfluidity predicted by Alonso-Matilla et al.'s (2016) model in Poiseuille flow in the zero-flow-rate limit.

differing geometries: Although up- and downstream conditions in Gachelin et al.'s (2013) device may have prevented the transition from occurring, it is unhindered in periodic channels where only the lateral wall spacing plays a role.

5. OTHER ACTIVE MATTER SYSTEMS

5.1. Cytoskeletal Extracts

Active fluids and materials abound in biological systems besides the oft-studied case of microswimmer suspensions. One fascinating example is the cell cytoskeleton (Mofrad 2009), which comprises cross-linked polymeric elastic filaments such as F-actin and microtubules (MTs). The activity of this network arises from the work performed by various ATP-powered molecular enzymes on the filaments for functions such as cell division, locomotion, or intracellular transport. Although the bulk characterization of these materials is not practical, the cytoskeleton can be probed in vivo using microrheological techniques (Wirtz 2009).
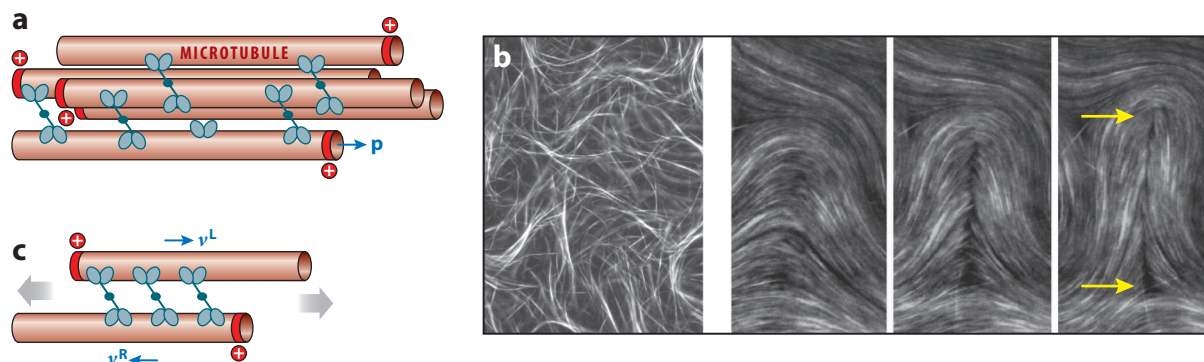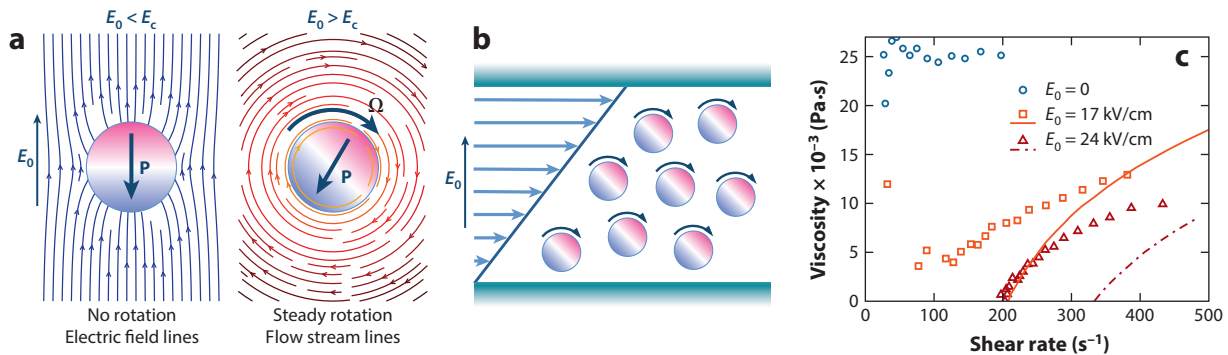
Figure 10

(*a*) Mechanism for extensile stress production in microtubule (MT)/motor-protein solutions. Multiheaded kinesin clusters marching along the polar MTs inside a bundle cause MTs of opposite polarities to slide in opposite directions, resulting in the bundle being extended. (*b*) Sanchez et al.'s (2012) experiments on the same system. The extension of MT bundles causes buckling instabilities and unstable transport. In the dense nematic phase, the dynamics are driven by the motion and interaction of active orientational defects (*yellow arrows*). Adapted from Shelley (2016).

Cytoskeletal extracts provide a simpler platform for studying the effects of ATP-driven activity on internal cellular mechanics. In recent experiments, Suzuki et al. (2017) visualized the dynamics in small liquid droplets containing *Xenopus* egg extract and reported the emergence of circular streaming flows attributed to the activity of kinesin motors on MTs. Using purified extracts, one can gain fundamental insight into MT–molecular motor interactions and their rheological consequences, as in the remarkable system proposed by Sanchez et al. (2012) (**Figure 10**). In their experiments, bundles of multiple MTs, which are polar elastic filaments with nominal plus and minus ends, are first assembled using a depletant agent. Multiheaded clusters composed of kinesin motors that bind to the polar MTs and walk towards their plus ends in the presence of ATP are used to induce the relative sliding of filaments of opposite polarities, causing the bundle to extend, which in turn exerts an extensile stresslet on the fluid (Shelley 2016) (**Figure 10*a***). In dilute systems, this extension results in the buckling and destruction of the bundles, which reform spontaneously, leading to unsteady chaotic dynamics. In dense nematic phases, large-scale correlated motions are observed that appear to be driven by the active motion of orientational defects (DeCamp et al. 2015, Gao et al. 2015) (**Figure 10*b***).

As in the case of bacterial suspensions, the chaotic motions observed in bulk systems can be stabilized and harnessed to drive steady unidirectional flows in microfluidic periodic channels with lengths up to 1 m (Wu et al. 2017). The strong phenomenological resemblance that these dynamics bear with spontaneous flows in bacterial suspensions hints at a similar rheology. It is indeed easy to imagine how an extending MT bundle orienting in an applied shear flow could drive a reduction in viscosity by the same effect as slender pushers (**Figure 4**), and existing hydrodynamic theories of MT/motor-protein suspensions give credit to this mechanism (Gao et al. 2015). This hypothesis is also consistent with observations of the microstructure in Wu et al.'s (2017) experiments, where alignment of the MTs with the self-induced flow was visible in the near-wall region. Standard rheological measurements of these active fluids have yet to be performed.

5.2. Quincke Rotors

Another way that suspended particles can modify the effective rheology is by exerting torques on the fluid. Although biological swimmers are typically torque free, with notable exceptions such

Figure 11

(*a*) Quincke electrorotation of an isolated particle. In weak fields ($E_0 < E_c$), a weakly conducting particle ($\tau_p > \tau_f$) acquires an induced dipole moment that is antiparallel with the field. As the field exceeds the critical value E_c, spontaneous rotation occurs at a constant angular velocity $\boldsymbol{\Omega}$ with a steady dipole moment that forms an angle with the field. (*b*) Under an applied shear flow, particle angular velocities align on average with the vorticity direction, causing a reduction in viscosity. (*c*) Viscosity measurements in a suspension of polymethyl methacrylate particles in oil (volume fraction 22%) in a circular Couette device under various field strengths (Lobry & Lemaire 1999), showing the reduction in viscosity. The solid and dashed lines show a theoretical prediction based on a dilute assumption.

as gravitactic microorganisms (Kessler 1986, Pedley & Kessler 1990) and magnetotatic bacteria (Blakemore 1982, Waisbord et al. 2016), synthetic microrotors subject to an external torque can be realized experimentally and indeed show interesting rheological properties. One such system is a suspension of weakly conducting dielectric particles suspended in a dielectric liquid under an applied electric field $\mathbf{E}_0$. In strong fields, such particles can start spontaneously spinning around an axis perpendicular to the field by an effect known as Quincke electrorotation (Quincke 1896). This effect, illustrated in **Figure 11**, occurs when the charge relaxation time τ_p of the particle is greater than that τ_f of the fluid, where $\tau = \varepsilon/\sigma$ is the ratio of the dielectric permittivity to the electric conductivity. The electrostatic dipole $\mathbf{P}$ induced inside the particle is then antiparallel with the applied field, which, when perturbed, results in an electric torque $\mathbf{L} = 4\pi\varepsilon_f\mathbf{P} \times \mathbf{E}_0$ that tries to align $\mathbf{P}$ with $\mathbf{E}_0$. However, the dipole moment does not follow the particle's rigid body rotation as charge from the bulk continues to accumulate and privileges the antiparallel orientation. The balance of these two effects results in a steady state where the particle rotates at a constant angular velocity $\boldsymbol{\Omega} = \mathbf{L}/8\pi\eta_0 a^3$, whereas the dipole moment forms an angle with the field direction (**Figure 11a**). A theoretical analysis of this problem using Melcher & Taylor's (1969) leaky dielectric model predicts the transition to electrorotation as a supercritical linear instability of the equilibrium state above a critical field strength (Jones 1984, Das & Saintillan 2013), with a steady angular velocity whose magnitude is given by

$$|\boldsymbol{\Omega}| = \frac{1}{\tau_{MW}}\sqrt{\left(\frac{E_0}{E_c}\right)^2 - 1}, \quad \text{with} \quad E_c = \sqrt{\frac{2\eta_0}{\varepsilon_f\tau_{MW}(\chi_\infty - \chi_0)}}. \qquad 17.$$

Here $\tau_{MW} = (\varepsilon_p + 2\varepsilon_f)/(\sigma_p + 2\sigma_f)$ is the Maxwell–Wagner time or characteristic timescale for polarization of the particle, and $\chi_0 = (\sigma_p - \sigma_f)/(\sigma_p + 2\sigma_f)$ and $\chi_\infty = (\varepsilon_p - \varepsilon_f)/(\varepsilon_p + 2\varepsilon_f)$ denote the low- and high-frequency Clausius–Mossotti factors, respectively (Jones 2005). The direction of rotation is perpendicular to the applied field ($\boldsymbol{\Omega} \cdot \mathbf{E}_0 = 0$) but is otherwise arbitrary.

When placed in an applied shear flow $\mathbf{U}(\mathbf{x}) = \dot{\gamma}y\hat{\mathbf{x}}$, the axis of rotation of the particles tends to align with the imposed vorticity (**Figure 11b**). In this configuration, particles spin at an angular

velocity that exceeds that of the imposed flow and thus tend to decrease the resistance to flow. This amounts to a reduction in the effective shear viscosity, which can be estimated in the dilute limit based on Batchelor's theory for the particle stress (Batchelor 1970b, Brenner 1970, Jibuti et al. 2012):

$$\eta_r = \frac{\sigma_{xy} + \Sigma_{xy}^p}{\eta_0 \dot{\gamma}} = 1 + \frac{5}{2}\phi + \frac{3}{2}\phi\,\Theta, \quad \text{with} \quad \Theta = \frac{L_z}{4\pi a^3 \eta_0 \dot{\gamma}} = 1 + \frac{\Omega_z}{\dot{\gamma}/2}. \qquad 18.$$

For torque-free particles ($L_z = 0$), the angular velocity is well known to be half the flow vorticity ($\Omega_z = -\dot{\gamma}/2$), so that $\Theta = 0$ and Equation 18 reduces to the classic Einstein result for a dilute sphere suspension (Guazzelli & Morris 2012). For Quincke rotors, the angular velocity is enhanced by the electric torque so that $\Theta < 0$, and a decrease in η_r is expected. This prediction was confirmed by Lobry & Lemaire (1999), who performed viscosity measurements in a circular Couette device (**Figure 11c**): Increasing field strength beyond the critical value was indeed shown to cause a dramatic decrease in viscosity. A similar effect was also reported in pressure-driven Poiseuille flow, where the application of a transverse electric field produces an increase in flow rate at a fixed pressure gradient (Lemaire et al. 2006, Peters et al. 2010). Curiously, the data of **Figure 11c** show a low-shear-rate viscosity that appears to become zero in strong fields, indicating an apparent transition to superfluidity akin to that observed in bacterial suspensions. This transition suggests once again the possible emergence of spontaneous flows, which have yet to be observed. Theoretical calculations for a pair of spheres indeed suggest that particle–particle interactions can lead to the synchronization of angular motions (Das & Saintillan 2013), and spontaneous collective dynamics have been reported in confined 2D suspensions of Quincke rotors (Bricard et al. 2013, 2015). No detailed data exist, however, on microstructural dynamics in bulk systems, whether in shear or quiescent conditions.

SUMMARY POINTS

1. The ability of microswimmers to generate fluid flows on the microscale as a result of self-propulsion enables them to modify their macroscopic rheological response in unusual ways. The nature of this response hinges on the details of propulsion (pusher versus puller) and on the particle configurations under flow, which result from the balance of shear alignment and orientation decorrelation mechanisms.

2. In slender pusher suspensions such as motile bacteria, this coupling leads to an effective decrease in the viscosity of the system in weak flows, which can even reach zero in certain geometries.

3. This apparent transition to superfluidity has wide-ranging consequences in semi-dilute and dense suspensions and underlies the emergence of spontaneous flows in confinement and of chaotic collective motion in bulk systems.

4. The finite relaxation time of particle orientations also confers viscoelastic properties on suspensions in unsteady flows, with pushers displaying stress overshoots at the startup of shear flow and negative stress undershoots after the flow has stopped.

DISCLOSURE STATEMENT

The author is not aware of biases that might be perceived as affecting the objectivity of this review.

ACKNOWLEDGMENTS

LITERATURE CITED

Alizadeh PA, Saintillan D. 2011. Instability regimes in flowing suspensions of swimming micro-organisms *Phys. Fluids* 23:011901

Alonso-Matilla R, Ezhilan B, Saintillan D. 2016. Microfluidic rheology of active particle suspensions: kinetic theory. *Biomicrofluidics* 10:043505

Alt W. 1980. Biased random walk models for chemotaxis and related diffusion approximations. *J. Math. Biol.* 9:147–77

Altschuler E, Miño G, Pérez-Penichet C, del Río L, Lindner A, et al. 2013. Flow-controlled densification and anomalous dispersion of *E. coli* through a constriction. *Soft Matter* 9:1864–70

Baskaran A, Marchetti MC. 2009. Statistical mechanics and hydrodynamics of bacterial suspensions. *PNAS* 106:15567–72

Batchelor GK. 1970a. Slender-body theory for particles of arbitrary cross-section in Stokes flow. *J. Fluid Mech.* 44:419–40

Batchelor GK. 1970b. The stress system in a suspension of force-free particles. *J. Fluid Mech.* 41:545–70

Batchelor GK. 1971. The stress generated in a non-dilute suspension of elongated particles by pure straining motion. *J. Fluid Mech.* 46:813–29

Batchelor GK. 1974. Transport properties of two-phase materials with random structure. *Annu. Rev. Fluid Mech.* 6:227–55

Bearon RN, Hazel AL. 2015. The trapping in high-shear regions of slender bacteria undergoing chemotaxis in a channel. *J. Fluid Mech.* 771:R3

Bearon RN, Pedley TJ. 2000. Modelling run-and-tumble chemotaxis in a shear flow. *Bull. Math. Biol.* 62:775

Bechtel TM, Khair AS. 2017. Linear viscoelasticity of a dilute active suspension. *Rheol. Acta* 56:149–60

Berg HC. 1993. *Random Walks in Biology*. Princeton, NJ: Princeton Univ. Press

Berg HC. 2004. *E. coli in Motion*. New York: Springer-Verlag

Berke AP, Turner L, Berg HC, Lauga E. 2008. Hydrodynamic attraction of swimming microorganisms by surfaces. *Phys. Rev. Lett.* 101:038102

Bianchi S, Saglimbeni F, Di Leonardo R. 2017. Holographic imaging reveals the mechanism of wall entrapment in swimming bacteria. *Phys. Rev. X* 7:011010

Blake JR. 2001. Fluid mechanics of ciliary propulsion. In *Computational Modeling in Biological Fluid Dynamics*, ed. LJ Fauci, S Gueron, pp. 1–51. New York: Springer

Blakemore RP. 1982. Magnetotactic bacteria. *Annu. Rev. Microbiol.* 36:217–38

Bozorgi Y, Underhill PT. 2014. Large-amplitude oscillatory shear rheology of dilute active suspensions. *Rheol. Acta* 53:899–909

Brennen C, Winet H. 1977. Fluid mechanics of propulsion by cilia and flagella. *Annu. Rev. Fluid Mech.* 9:339–98

Brenner H. 1970. Rheology of a dilute suspension of dipolar spherical particles in an external field. *J. Colloid Interface Sci.* 32:141–58

Brenner H. 1974. Rheology of a dilute suspension of axisymmetric Brownian particles. *Int. J. Multiph. Flow* 1:195–341

Brenner H. 1980. A general theory of Taylor dispersion phenomena. *Physicochem. Hydrodyn.* 1:91–123

Brenner H, Condiff DW. 1974. Transport mechanics in systems of orientable particles. 4. Convective transport. *J. Colloid Interface Sci.* 47:199–264

Bretherton FP. 1962. The motion of rigid particles in a shear flow at low Reynolds number. *J. Fluid Mech.* 14:284–304

Bricard A, Caussin J-B, Das D, Savoie C, Chikkadi V, et al. 2015. Emergent vortices in populations of colloidal rollers. *Nat. Commun.* 6:7470

Bricard A, Caussin J-B, Desreumaux N, Dauchot O, Bartolo D. 2013. Emergence of macroscopic directed motion in populations of motile colloids. *Nature* 503:95–98

Brotto T, Bartolo D, Saintillan D. 2015. Spontaneous flows in suspensions of active cyclic swimmers. *J. Nonlinear Sci.* 25:1125–39

Chattopadhyay S, Moldovan R, Yeung C, Wu XL. 2006. Swimming efficiency of bacterium *Escherichia coli*. *PNAS* 103:13712–17

Chen SB, Jiang L. 1999. Orientation distribution in a dilute suspension of fibers subject to simple shear flow. *Phys. Fluids* 11:2878–90

Chen SB, Koch DL. 1996. Rheology of dilute suspensions of charged fibers. *Phys. Fluids* 8:2792–807

Chengala A, Hondzo M, Sheng J. 2013. Microalga propels along vorticity direction in a shear flow. *Phys. Rev. E* 87:052704

Cisneros LH, Cortez R, Dombrowski C, Goldstein RE, Kessler JO. 2007. Fluid dynamics of self-propelled microorganisms, from individuals to concentrated populations. *Exp. Fluids* 43:737–53

Clément E, Lindner A, Douarche C, Auradou H. 2016. Bacterial suspensions under flow. *Eur. Phys. J. Spec. Top.* 225:2389–406

Creppy A, Plouraboué F, Praud O, Druart X, Cazin S, et al. 2016. Symmetry-breaking phase transitions in highly concentrated semen. *J. R. Soc. Interface* 13:20160575

Darnton NC, Turner L, Rojevsky S, Berg HC. 2007. On torque and tumbling in swimming *Escherichia coli*. *J. Bacteriol.* 189:1756–64

Das D, Saintillan D. 2013. Electrohydrodynamic interaction of spherical particles under Quincke rotation. *Phys. Rev. E* 87:043014

de Gennes PG, Prost J. 2002. *The Physics of Liquid Crystals*. Oxford, UK: Oxford Univ. Press

DeCamp SJ, Redner GS, Baskaran A, Hagan MF, Dogic Z. 2015. Orientational order of motile defects in active nematics. *Nat. Mater.* 14:1110–15

Denissenko P, Kantsler V, Smith DJ, Kirkman-Brown J. 2012. Human spermatozoa migration in microchannels reveals boundary-following navigation. *PNAS* 109:8007–10

Di Leonardo R, Angelani L, Dell'Arciprete D, Ruocco G, Iebba V, et al. 2010. Bacterial ratchet motors. *PNAS* 107:9541–45

Doi M, Edwards SF. 1986 *The Theory of Polymer Dynamics*. Oxford, UK: Oxford Univ. Press

Drescher K, Dunkel J, Cisneros LH, Ganguly S, Goldstein RE. 2011. Fluid dynamics and noise in bacterial cell–cell and cell–surface scattering. *PNAS* 108:10940–45

Drescher K, Goldstein RE, Michel N, Polin M, Tuval I. 2010. Direct measurement of the flow field around swimming microorganisms. *Phys. Rev. Lett.* 105:168101

Ebbens SJ, Howse JR. 2010. In the pursuit of propulsion at the nanoscale. *Soft Matter* 6:726–38

Elgeti J, Winkler RG, Gompper G. 2015. Physics of microswimmers—single particle motion and collective behavior: a review. *Rep. Prog. Phys.* 78:056601

Ericksen JL. 1962. Hydrostatic theory of liquid crystals. *Arch. Ration. Mech. Anal.* 9:371–78

Ewoldt RH, Bharadwaj NA. 2013. Low-dimensional intrinsic material functions for nonlinear viscoelasticity. *Rheol. Acta* 52:201–19

Ezhilan B, Alizadeh Pahlavan A, Saintillan D. 2012. Chaotic dynamics and oxygen transport in thin films of aerotactic bacteria. *Phys. Fluids* 24:091701

Ezhilan B, Saintillan D. 2015. Transport of a dilute active suspension in pressure-driven channel flow. *J. Fluid Mech.* 777:482–522

Figueroa-Morales N, Miño G, Rivera A, Caballero R, Clément E, et al. 2015. Living on the edge: transfer and traffic of *E. coli* in a confined flow. *Soft Matter* 11:6284–93

Foffano G, Lintuvuori JS, Morozov AN, Stratford K, Cates ME, Marenduzzo D. 2012a. Bulk rheology and microrheology of active fluids. *Eur. Phys. J. E* 35:98

Foffano G, Lintuvuori JS, Stratford K, Cates ME, Marenduzzo D. 2012b. Colloids in active fluids: anomalous microrheology and negative drag. *Phys. Rev. Lett.* 109:028103

Fürthauer S, Neef M, Grill SW, Kruse K, Jülicher F. 2012. The Taylor–Couette motor: spontaneous flows of active polar fluids between two coaxial cylinders. *New J. Phys.* 14:023001

Fürthauer S, Ramaswamy S. 2013. Phase-synchronized state of oriented active fluids. *Phys. Rev. Lett.* 111:238102

Gachelin J, Miño G, Berthet H, Landner A, Rousselet A, Clément E. 2013. Non-Newtonian viscosity of *Escherichia coli* suspensions. *Phys. Rev. Lett.* 110:268103

Gao T, Blackwell R, Glaser M, Betterton N, Shelley M. 2015. Multiscale polar theory of microtubule and motor-protein assemblies. *Phys. Rev. Lett.* 114:048101

Garcia M, Berti S, Peyla P, Rafaï S. 2011. Random walk of a swimmer in a low-Reynolds-number medium. *Phys. Rev. E* 83:035301

Ghose S, Adhikari R. 2014. Irreducible representations of oscillatory and swirling flows in active soft matter. *Phys. Rev. Lett.* 112:118102

Gibbs JG, Zhao YP. 2009. Autonomously motile catalytic nanomotors by bubble propulsion. *Appl. Phys. Lett.* 94:163104

Giomi L, Liverpool TB, Marchetti MC. 2010. Sheared active fluids: thickening, thinning, and vanishing viscosity. *Phys. Rev. E* 81:051908

Gluzman S, Karpeev DA, Berlyand LV. 2013. Effective viscosity of puller-like microswimmers: a renormalization approach. *J. R. Soc. Interface* 10:20130720

Goldstein RE. 2015. Green algae as model organisms for biological fluid dynamics. *Annu. Rev. Fluid Mech.* 47:343–75

Gray J, Hancock GJ. 1955. The propulsion of sea-urchin spermatozoa. *J. Exp. Biol.* 32:802–14

Guasto JS, Johnson KA, Gollub JP. 2010. Oscillatory flows induced by microorganisms swimming in two dimensions. *Phys. Rev. Lett.* 105:168102

Guazzelli E, Morris JF. 2012. *A Physical Introduction to Suspension Dynamics*. Cambridge, UK: Cambridge Univ. Press

Gyrya V, Lipnikov K, Aranson IS, Berlyand L. 2011. Effective shear viscosity and dynamics of suspensions of micro-swimmers from small to moderate concentrations. *J. Math. Biol.* 62:707–40

Haines BM, Sokolov A, Aranson IS, Berlyand L, Karpeev DA. 2009. Three-dimensional model for the effective viscosity of bacterial suspensions. *Phys. Rev. E* 80:041922

Hatwalne Y, Ramaswamy S, Rao M, Aditi Simha R. 2004. Rheology of active-particle suspensions. *Phys. Rev. Lett.* 92:118101

Heidenreich S, Hess S, Klapp SHL. 2011. Nonlinear rheology of active particle suspensions: insights from an analytical approach. *Phys. Rev. E* 83:011907

Hemingway EJ, Maitra A, Banerjee S, Marchetti MC, Ramaswamy S, et al. 2015. Active viscoelastic matter: from bacterial drag reduction to turbulent solids. *Phys. Rev. Lett.* 114:098302

Hinch EJ, Leal LG. 1972. The effect of Brownian motion on the rheological properties of a suspension of non-spherical particles. *J. Fluid Mech.* 52:683–712

Hinch EJ, Leal LG. 1976. Constitutive equations in suspension mechanics. Part 2. Approximate forms for a suspension of rigid particles affected by Brownian rotations. *J. Fluid Mech.* 76:187–208

Hope A, Croze OA, Poon WCK, Bees MA, Haw MD. 2016. Resonant alignment of microswimmer trajectories in oscillatory shear flows. *Phys. Rev. Fluids* 1:051201

Huang HF, Zahn M, Lemaire E. 2010. Continuum modeling of micro-particle electrorotation in Couette and Poiseuille flows—the zero spin viscosity limit. *J. Electrostat.* 68:345–59

Irving JH, Kirkwood JG. 1950. The statistical mechanical theory of transport processes. IV. The equations of hydrodynamics. *J. Chem. Phys.* 18:817–29

Ishikawa T, Pedley TJ. 2007. The rheology of a semi-dilute suspension of swimming model micro-organisms. *J. Fluid Mech.* 588:399–435

Jeffery GB. 1922. The motion of ellipsoidal particles immersed in a viscous fluid. *Proc. R. Soc. A* 102:161–79

Jibuti L, Rafaï S, Peyla P. 2012. Suspensions with a tunable effective viscosity: a numerical study. *J. Fluid Mech.* 693:345–66

Jones TB. 1984. Quincke rotation of spheres. *IEEE Trans. Ind. Appl.* IA-20:845–49

Jones TB. 2005. *Electromechanics of Particles*. Cambridge, UK: Cambridge Univ. Press

Kaiser A, Peshkov A, Sokolov A, ten Hagen B, Löwen H, Aranson IS. 2014. Transport powered by bacterial turbulence. *Phys. Rev. Lett.* 112:158101

Karmakar R, Gulvady R, Tirumkudulu MS, Venkatesh KV. 2014. Motor characteristics determine the rheological behavior of a suspension of microswimmers. *Phys. Fluids* 26:071905

Kasyap TV, Koch DL. 2012. Chemotaxis driven instability of a confined bacterial suspension. *Phys. Rev. Lett.* 108:038101

Kaya T, Koser H. 2012. Direct upstream motility in *E. coli. Biophys. J.* 102:1514–23

Kessler JO. 1986. Individual and collective dynamics of swimming cells. *J. Fluid Mech.* 173:191–205

Kim S, Karrila SJ. 2005. *Microhydrodynamics: Principles and Selected Applications*. Mineola, NY: Dover

Klindt GS, Friedrich BM. 2015. Flagellar swimmers oscillate between pusher- and puller-type swimming. *Phys. Rev. E* 92:063019

Koch DL, Subramanian G. 2011. Collective hydrodynamics of swimming microorganisms: living fluids. *Annu. Rev. Fluid Mech.* 43:637–59

Krieger IM, Dougherty TJ. 1959. A mechanism for non-Newtonian flow in suspensions of rigid spheres. *Trans. Soc. Rheol.* 3:137–52

Lauga E. 2016. Bacterial hydrodynamics. *Annu. Rev. Fluid Mech.* 48:105–30

Lauga E, DiLuzio WR, Whitesides GM, Stones HA. 2006. Swimming in circles: motion of bacteria near solid boundaries. *Biophys. J.* 90:400–12

Lauga E, Michelin S. 2016. Stresslets induced by active swimmers. *Phys. Rev. Lett.* 117:148001

Lauga E, Powers TR. 2009. The hydrodynamics of swimming microorganisms. *Rep. Prog. Phys.* 72:096601

Lemaire E, Lobry L, Pannacci N. 2006. Flow rate increased by electrorotation in a capillary. *J. Electrostat.* 64:586–90

Lemaire E, Lobry LN, Pannacci F, Peters F. 2008. Viscosity of an electro-rheological suspension with internal rotations. *J. Rheol.* 52:769–85

Leoni M, Liverpool TB. 2014. Synchronization and liquid crystalline order in soft active fluids. *Phys. Rev. Lett.* 112:148104

Liao Q, DeLisa MP, Koch D, Wu M. 2007. Pair velocity correlations among swimming *Escherichia coli* bacteria are determined by force-quadrupole hydrodynamic interactions. *Phys. Fluids* 19:061701

Lighthill J. 1975. *Mathematical Biofluiddynamics*. Philadelphia: Soc. Ind. Appl. Math.

Lobry L, Lemaire E. 1999. Viscosity decrease induced by a DC electric field in a suspension. *J. Electrostat.* 47:61–69

López HM, Gachelin J, Douarche C, Auradou H, Clément E. 2015. Turning bacteria suspensions into superfluids. *Phys. Rev. Lett.* 115:028301

Lushi E, Wioland H, Goldstein RE. 2014. Fluid flows created by swimming bacteria drive self-organization in confined suspensions. *PNAS* 111:9733–38

Manela A, Frankel I. 2003. Generalized Taylor dispersion in suspensions of gyrotactic swimming microorganisms. *J. Fluid Mech.* 490:99–127

Marchetti MC, Joanny JF, Ramaswamy S, Liverpool TB, Prost J, et al. 2013. Hydrodynamics of soft active matter. *Rev. Mod. Phys.* 85:1143–89

Marcos Fu HC, Powers TR, Stocker R. 2012. Bacterial rheotaxis. *PNAS* 109:4780–85

McDonnell AG, Gopesh TC, Lo J, O'Bryan M, Yeo LY, et al. 2015. Motility induced changes in viscosity of suspensions of swimming microbes in extensional flows. *Soft Matter* 11:4658–68

Melcher JR, Taylor GI. 1969. Electrohydrodynamics: a review of the role of interfacial shear stresses. *Annu. Rev. Fluid Mech.* 1:111–46

Michelin S, Lauge E, Bartolo D. 2013. Spontaneous autophoretic motion of isotropic particles. *Phys. Fluids* 25:061701

Mofrad MRK. 2009. Rheology of the cytoskeleton. *Annu. Rev. Fluid Mech.* 41:433–53

Moradi M, Najafi A. 2015. Rheological properties of a dilute suspension of self-propelled particles. *Europhys. Lett.* 109:24001

Moran JL, Posner JD. 2017. Phoretic self-propulsion. *Annu. Rev. Fluid Mech.* 49:511–40

Mussler M, Rafaï S, Peyla P, Wagner C. 2013. Effective viscosity of non-gravitactic *Chlamydomonas reinhardtii* microswimmer suspensions. *Europhys. Lett.* 101:54004

Nambiar S, Nott PR, Subramanian G. 2017. Stress relaxation in a dilute bacterial suspension. *J. Fluid Mech.* 812:41–64

Pagonabarraga I, Llopis I. 2013. The structure and rheology of sheared model swimmer suspensions. *Soft Matter* 9:7174–84

Patteson AE, Gopinath A, Purohit PK, Arratia PE. 2016. Particle diffusion in active fluids is non-monotonic in size. *Soft Matter* 12:2365–72

Paxton WF, Kistler KC, Olmeda CC, Sen A, St. Angelo SK, et al. 2004. Catalytic nanomotors: autonomous movement of striped nanorods. *J. Am. Chem. Soc.* 126:13424–31

Pedley TJ, Kessler JO. 1990. A new continuum model for suspensions of gyrotactic micro-organisms. *J. Fluid Mech.* 212:155–82

Peng Y, Lai L, Tai YS, Zhang K, Xu X, Cheng X. 2016. Diffusion of ellipsoids in bacterial suspensions. *Phys. Rev. Lett.* 116:068303

Peters F, Lobry L, Lemaire E. 2010. Pressure-driven flow of a micro-polar fluid: measurement of the velocity profile. *J. Rheol.* 54:311–25

Petrie CJS. 1999. The rheology of fibre suspensions. *J. Non-Newton. Fluid Mech.* 87:369–402

Potomkin M, Ryan SD, Berlyand L. 2016. Effective rheological properties in semidilute bacterial suspensions. *Bull. Math. Biol.* 78:580–615

Pozrikidis C. 1992. *Boundary Integral and Singularity Methods for Linearized Viscous Flow*. Cambridge, UK: Cambridge Univ. Press

Purcell EM. 1977. Life at low Reynolds number. *Am. J. Phys.* 45:3–11

Quincke G. 1896. Über Rotationen im constanten elektrischen Felde. *Ann. Phys. Chem.* 59:417–86

Rafaï S, Jibuti L, Peyla P. 2010. Effective viscosity of microswimmer suspensions. *Phys. Rev. Lett.* 104:098102

Ramaswamy S. 2010. The mechanics and statistics of active matter. *Annu. Rev. Condens. Matter Phys.* 1:323–45

Rusconi R, Guasto JS, Stocker R. 2014. Bacterial transport suppressed by fluid shear. *Nat. Phys.* 10:212–17

Ryan SD, Haines BM, Berlyand L, Ziebert F, Aranson IS. 2011. Viscosity of bacterial suspensions: hydrodynamic interactions and self-induced noise. *Phys. Rev. E* 83:050904

Saintillan D. 2010a. Extensional rheology of active suspensions. *Phys. Rev. E* 81:056307

Saintillan D. 2010b. The dilute rheology of swimming suspensions: a simple kinetic model. *Exp. Mech.* 50:1275–81

Saintillan D, Shelley MJ. 2008. Instabilities and pattern formation in active particle suspensions: kinetic theory and continuum simulations. *Phys. Rev. Lett.* 100:178103

Saintillan D, Shelley MJ. 2012. Emergence of coherent structures and large-scale flows in motile suspensions. *J. R. Soc. Interface* 9:571–85

Saintillan D, Shelley MJ. 2015. Theory of active suspensions. In *Complex Fluids in Biological Systems*, ed. SE Spagnolie, pp. 319–55. New York: Springer

Sanchez T, Chen D, DeCamp S, Heymann M, Dogic Z. 2012. Spontaneous motion in hierarchically assembled active matter. *Nature* 491:431–34

Saracco GP, Gonnella G, Marenduzzo D, Orlandini E. 2011. Shearing self-propelled suspensions: arrest of coarsening and suppression of giant density fluctuations. *Phys. Rev. E* 84:031930

Schaar K, Zöttl A, Stark H. 2015. Detention times of microswimmers close to surfaces: influence of hydrodynamic interactions and noise. *Phys. Rev. Lett.* 115:038101

Secchi E, Rusconi R, Buzzaccaro S, Salek MM, Smriga S, et al. 2016. Intermittent turbulence in flowing bacterial suspensions. *J. R. Soc. Interface* 13:20160175

Shelley MJ. 2016. The dynamics of microtubule/motor-protein assemblies in biology and physics. *Annu. Rev. Fluid Mech.* 48:487–506

Simha RA, Ramaswamy S. 2002. Hydrodynamic fluctuations and instabilities in ordered suspensions of self-propelled particles. *Phys. Rev. Lett.* 89:058101

Sokolov A, Aranson IS. 2009. Reduction of viscosity in suspension of swimming bacteria. *Phys. Rev. Lett.* 103:148101

Sokolov A, Aranson IS. 2012. Physical properties of collective motion in suspensions of bacteria. *Phys. Rev. Lett.* 109:248109

Solon AP, Stenhammar J, Wittkowski R, Kardar M, Kafri Y, et al. 2015. Pressure and phase equilibria in interacting active Brownian spheres. *Phys. Rev. Lett.* 114:198301

Spagnolie SE, Lauga E. 2012. Hydrodynamics of self-propulsion near boundaries: predictions and accuracy of far-field approximations. *J. Fluid Mech.* 700:105–47

Subramanian G, Koch DL. 2009. Critical bacterial concentration for the onset of collective swimming. *J. Fluid Mech.* 632:359–400

Suzuki K, Miyazaki M, Takagi J, Itabashi T, Ishiwata S. 2017. Spatial confinement of active microtubule networks induces large-scale rotational cytoplasmic flow. *PNAS* 114:2922–27

Takatori SC, Brady JF. 2017. Superfluid behavior of active suspensions from diffusive stretching. *Phys. Rev. Lett.* 118:018003

Takatori SC, Wen Y, Brady JF. 2014. Swim pressure: stress generation in active matter. *Phys. Rev. Lett.* 113:028103

Theillard M, Alonso-Matilla R, Saintillan D. 2017. Geometric control of active collective motion. *Soft Matter* 13:363–75

Turner L, Ryu WS, Berg HC. 2000. Real-time imaging of fluorescent flagellar filaments. *J. Bacteriol.* 182:2793–801

Waisbord N, Lefèvre CT, Bocquet L, Ybert C, Cottin-Bizonne C. 2016. Destabilization of a flow focused suspension of magnetotactic bacteria. *Phys. Rev. Fluids* 1:053203

Wang J. 2013. *Nanomachines: Fundamentals and Applications*. Weinheim, Ger.: Wiley-VCH

Wioland H, Lushi E, Goldstein RE. 2015. Directed collective motion of bacterial under channel confinement. *New J. Phys.* 18:075002

Wioland H, Woodhouse FG, Dunkel J, Kessler JO, Goldstein RE. 2013. Confinement stabilizes a bacterial suspension into a spiral vortex. *Phys. Rev. Lett.* 110:268102

Wirtz D. 2009. Particle-tracking rheology of living cells: principles and applications. *Annu. Rev. Biophys.* 38:301–26

Woodhouse FG, Goldstein RE. 2012. Spontaneous circulation of confined active suspensions. *Phys. Rev. Lett.* 109:168105

Wu K-T, Hishamunda JB, Chen DTN, DeCamp SJ, Chang Y-W, et al. 2017. Transition from turbulent to coherent flows in confined three-dimensional active fluids. *Science* 355(6331):2017

Wu XL, Libchaber A. 2000. Particle diffusion in a quasi-two-dimensional bacterial bath. *Phys. Rev. Lett.* 84:3017–20

Yan W, Brady JF. 2015. The force on a boundary in active matter. *J. Fluid Mech.* 785:R1